ADVANCED MATERIALS
www.advmat.de

Artesunate Nanoplatform Targets the Serine–MAPK Axis in Cancer-Associated Fibroblasts to Reverse Photothermal Resistance in Triple-Negative Breast Cancer

Dongdong Zheng, Jiaqi Yan, Xuejiao Liu, Zhiming Zhang, Anqi Jin, Yue Zhao, Lu Bai, Mengyao Quan, Xiuzhu Qi, Bin Fu, Zhigang Wu, Jin Zhou, Han Han, Ziqi Wang, Shiyu Wang, Chaoqiang Deng, Weijian Sun, Cai Chang,* Shichong Zhou,* and Hongbo Zhang**

Cancer-associated fibroblasts (CAFs) play a pivotal role in inducing photothermal therapy (PTT) resistance of triple-negative breast cancer (TNBC), but with unclear mechanism. Herein, aminoethyl anisamide-modified nano-biomimetic low-density lipoprotein (A-aLDL) is used to target deliver the PTT agent and artesunate (ARS) to both CAFs and cancer cells. Though CAFs are sensitive to PTT and notably transition to heat-resistant phenotype, the formed protective barrier is destroyed by ARS. Subsequently, the outstanding anti-tumor effects are achieved through PTT in multiple models with such kind of combination therapy. Interestingly, the mechanism is discovered that serine metabolism plays a major role in CAF resistance through spatially omics. ARS disrupts serine homeostasis, thereby attenuating the cascade activity of GTPases in MAPK pathway. Meanwhile, MAP2K7 is the most potential target for sensitizing PTT. By integrating ARS with PTT agents, the serine-MAPK axis in CAFs is successfully modulated, thereby overcoming PTT resistance in TNBC therapy.

1. Introduction

Photothermal therapy (PTT) is a promising thermal treatment modality for tumor, especially in combination with tumor-targeting nanomaterials, which can achieve precise and remote tumor treatment.[1–3] Unlike laser interstitial thermal therapy (LITT), which is applied clinically to deep organs.[4] PTT has been indicated to be advantageous for the noninvasive treatment of superficial organ tumors, particularly triple-negative breast cancer (TNBC). Indocyanine green (ICG)-mediated PTT is used in clinical trial to treat metastatic breast cancer.[5] However, similar to the challenges that occur with chemotherapy and immunal therapy,

D. Zheng, Z. Zhang, A. Jin, L. Bai, M. Quan, X. Qi, J. Zhou, Z. Wang, S. Wang, C. Chang, S. Zhou
Department of Ultrasound
Fudan University Shanghai Cancer Center
Shanghai 200032, P. R. China
E-mail: zhengdongdong@fudan.edu.cn; changc61@163.com; sczhou@fudan.edu.cn

J. Yan, W. Sun, H. Zhang
Joint Centre of Translational Medicine, Wenzhou Key Laboratory of Interdiscipline and Translational Medicine
the First Affiliated Hospital of Wenzhou Medical University
Wenzhou 325000, P. R. China
E-mail: hongbo.zhang@abo.fi

The ORCID identification number(s) for the author(s) of this article can be found under https://doi.org/10.1002/adma.202502617

DOI: 10.1002/adma.202502617

X. Liu, B. Fu
Institutes of Biomedical Sciences and Department of Chemistry
Fudan University
Shanghai 200032, P. R. China

Z. Wu, H. Han, C. Deng
Department of Thoracic Surgery and State Key Laboratory of Genetic Engineering
Shanghai 200032, P. R. China

J. Yan, Y. Zhao, H. Zhang
Pharmaceutical Sciences Laboratory
Åbo Akademi University
Turku FI-00520, Finland

J. Yan, H. Zhang
Turku Bioscience Center
University of Turku and Åbo Akademi University
Turku FI-00520, Finland

Y. Zhao, Z. Wu, H. Han, C. Deng
Institute of Thoracic Oncology
Fudan University
Shanghai 200032, P. R. China

D. Zheng, C. Chang
Department of Oncology, Shanghai Medical College
Fudan University
Shanghai 200032, P. R. China

tumor resistance to PTT remains a significant hurdle for its clinical translation. While, unlike other treatments, the PTT resistance mechanism in TNBC is unclear.

In response to therapy, the cells in tumor inevitably evoke a stress response, and self-regulate the tumor microenvironment to cope with the stress, thus develop resistance in tumor.[6–8] Cancer-associated fibroblasts (CAFs) can be activated under traumatic stress to produce various cytokines and activating pathways that promote tumor fibrosis and resistance to treatment.[9–12] For example, in chemotherapy-resistant tumor phenotypes, MAPK pathway is abnormally activated.[13–15] And the abnormal activation of the MAPK pathway, particularly the IL-6/STAT3 signaling axis, intensifies intratumoral fibrosis.[16–18] Additionally, the SAPK/JNK signaling axis in the MAPK pathway plays a regulatory role, enhancing the tolerance of CAFs to oxidative stress and thereby bolstering fibroblast resilience to external stimuli.[19–23] Therefore, the MAPK pathway is an important pathway for the occurrence of fibrosis after tumor stress, which is a potential target for addressing tumor PTT resistance.

TNBC is a pathological type of breast cancer with complex and heterogeneous tumor microenvironments,[24,25] different stresses trigger different regulatory mechanisms in TNBC. Therefore, understanding the heat resistance mechanisms triggered by photothermal stress in TNBC is crucial for promoting the clinical translation of PTT. CAFs have the potential to promote tumor heat resistance but owing to their heterogeneity,[26,27] it is important to figure out which type of CAF regulate heat resistance. In our previous study,[27] we identified that the proportion of extracellular matrix CAFs (ECM CAFs) significantly increased in tumors after PD-1 monoclonal antibody treatment. Moreover, artesunate (ARS), a STAT3 inhibitor, was shown to effectively and specifically inhibit CAFs, particularly pronounced in ECM CAFs.[27] Therefore, ARS is a potential drug for regulating the ECM CAFs to conquer the heat resistance in TNBC.

In this study, an ARS and ICG co-loaded biomimetic low-density lipoprotein (LDL) was conjugated with aminoethyl anisamide (AEAA) to specially inhibit ECM CAFs and cancer cells in TNBC. Spatial transcription sequencing and spatial metabolic sequencing were utilized to evaluate the role of ECM CAFs in PTT resistance of TNBC. Further, the mechanism of ARS regulates serine homeostasis and GTPases activity of MAPK pathway in CAF cell was investigated. This study points to significant reasons for limiting the efficacy of ICG-mediated PTT in clinical trials, which paves the way to effectively treat TNBC in promoting clinical translational of PTT (**Scheme 1**).

2. Results

2.1. CAFs are Involved in Tumor Resistance to PTT

Previous investigations have illustrated the capacity of heat shock protein (HSP) inhibitors to increase the efficacy and sensitivity of PTT.[3,28–30] Consequently, the abundance of heat shock proteins has emerged as a prospective marker for evaluating the efficacy of tumor PTT. To assess the role of CAFs in PTT resistance in TNBC, we reanalyzed scRNA-seq data previously published by our group to assess heat shock protein expression across different cell clusters.[27] Compared with other clusters, CAFs presented higher heat shock mRNA levels (**Figure 1A**), suggesting that CAFs have greater heat tolerance. Furthermore, we evaluated free ICG-mediated PTT in a Balb/c nude mouse model: one group was coimplanted with human immortalized CAFs and MDA-MB-231 cells, and the other group was implanted with only MDA-MB-231 cells, and weaker therapeutic effects were observed in the coimplantation model mice within 12 days (Figure 1B). The tumor growth of co-implantation and cancer cell implantation alone did not produce a significant difference in volume within 12 days after implantation (Figure S1A, Supporting Information).These results directly indicate that CAFs are involved in PTT resistance. Additionally, the signature score analysis revealed that ECM CAFs better regulated the cellular heat acclimation than other clusters significantly (Figure S1B, Supporting Information). On the basis of the gene expression levels in each CAF subtype (Figure S1C, Supporting Information), we defined the CAF sbtype with high *Tnc* expression as ECM CAF.[31,32] Gene Ontology Biological Process (GOBP) revealed significant enrichment of the inflammatory response to wounding pathway in ECM CAFs (Figure S1D, Supporting Information). Similarly, the expression of ECM CAF markers was increased in Eo771 tumor treated with free ICG-mediated PTT compared to control group (Figure 1C; Figure S1E, Supporting Information). Given the high enrichment of the collagen fiber organization pathway in ECM CAFs, as expected, the tumor tissues presented a significant increase in ECM organization after PTT (Figure S1F, Supporting Information).

Overall, CAFs, especially ECM CAFs, play a key role in TNBC resistance to PTT.

2.2. A Dual-Targeting ARS Nanoplatform was Prepared to Specifically Inhibit CAFs to Sensitize them to PTT

ATF4 is an important marker of stress in CAFs.[33] Pseudotime analysis revealed that ECM CAFs and wound healing CAFs had increased *Atf4* expression levels (Figure S1G, Supporting Information). ARS has been reported to inhibit CAFs and sensitize tumors to therapy.[27,34,35] Therefore, PLGA (poly (lactic-co-glycolic acid))-loaded ARS was first tested and was found to reduce *Atf4* expression levels in both subtypes (Figure 1D). To further achieve sensitization to PTT, we developed a nanoplatform using LDL as a carrier to load ARS (aLDL@A), which was further surface modified by conjugation of anisamide (A-aLDL@A) and ICG (AI-aLDL@A) (Figure 1E). We used PEG2000 as the linker, with one end conjugated to the lipophilic-phase DSPE and the other end connected to AEAA. During the formation of the nanoplatform, the DSPE end becomes embedded within the nanocarrier, while AEAA remains exposed on the surface of the nanocarrier to exert its targeting effect on sigmar-1. Similarly, ICG is also exposed on the exterior of the nanocarrier through this configuration. After cellular internalization of the nanocarrier, NIR laser irradiation can effectively activate the ICG-mediated PTT effect. AEAA has affinity for the sigma-1 receptor, and literature reports indicate that CAFs express high levels of sigma-1 receptors.[35–38] Additionally, LDLs formed with an apob-100 backbone (aLDL) have increased affinity for tumor cells.[39–43] Therefore, this nanoplatform can simultaneously target TNBC cells and CAFs and specifically inhibit both types of cells. The developed nanoplatform was spherical with a particle diameter of

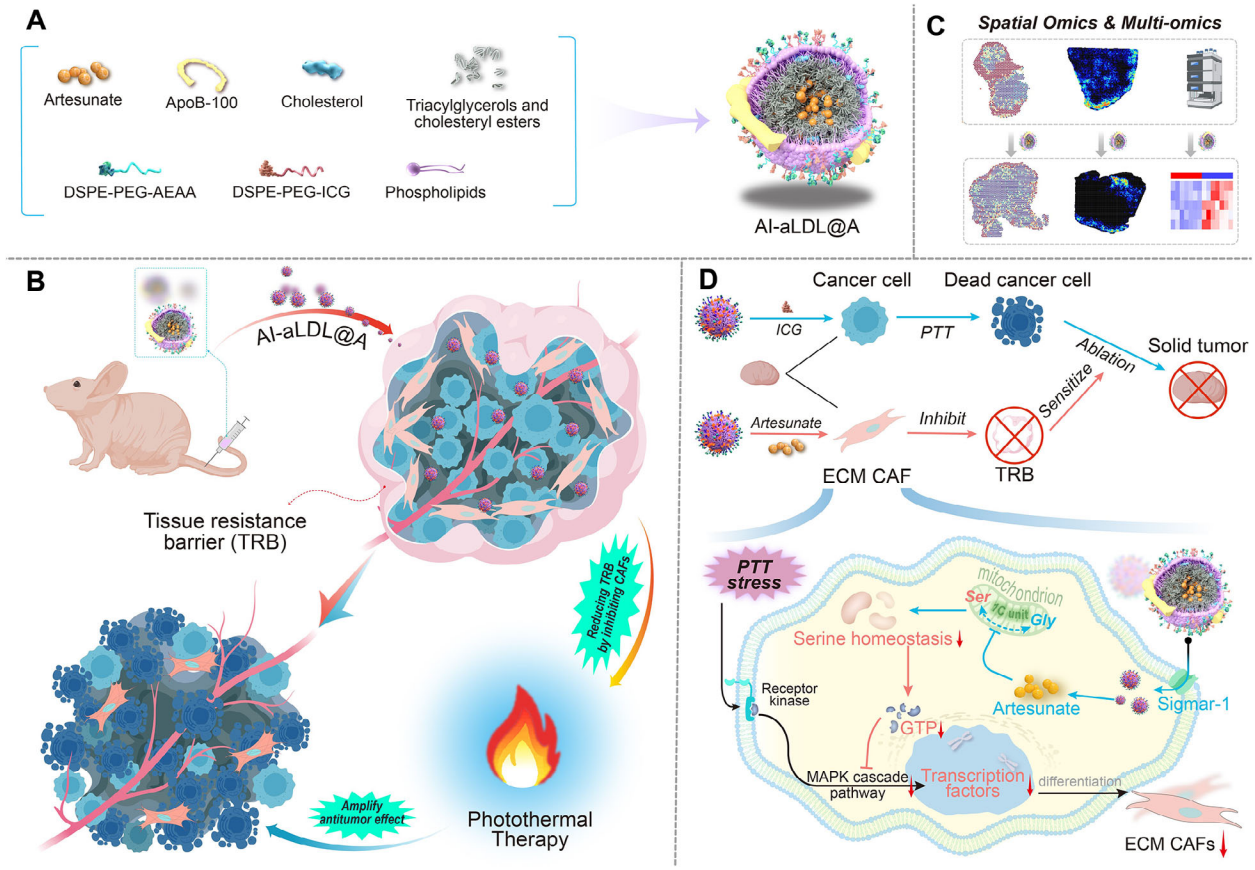

Scheme 1. Schematic illustration of this study outline. A) Schematic diagram of the components and structure of the artesunate nanoplatform (AI-aLDL@A). B) The artesunate nanoplatform effectively disrupts the CAF-mediated tissue resistance barrier (TRB), thereby significantly potentiating the in vivo photothermal therapy (PTT) efficacy. C) Spatial multi-omics and multi-omics sequencing assist in exploring the mechanism of the artesunate nanoplatform sensitizing PTT in TNBC. D) The artesunate nanoplatform selectively targets ECM CAF, functioning as a GTPase inhibitor through disruption of intracellular serine homeostasis. This metabolic intervention effectively suppresses MAPK cascade activity, which consequently inhibits PTT-induced CAF to ECM CAF differentiation. By attenuating this phenotypic transition, the nanoplatform significantly reduces the formation of TRB structure, ultimately enhancing tumor sensitivity to PTT.

≈60 nm (Figure 1F). No significant change in particle size was observed after LDL modification (Figure 1F). Nanoparticles exhibit a larger hydration volume in aqueous solutions due to solvent effects.[44] Moreover, hydrodynamic diameter monitoring revealed that the nanoplatform exhibited good stability over 24 h (Figure 1G; Figure S2A,B, Supporting Information). After surface modification with AEAA and ICG, the hydrodynamic diameter of AI-aLDL@A increased due to solvent effects. Both LDL@A and AI-aLDL@A displayed negative surface charges (Figure S2C, Supporting Information). Of note, the ARS nanoplatform had a longer storage period when stored in dry powder state at low temperature (Figure S2D, Supporting Information). Furthermore, the critical aggregation concentration (CAC) of the nanocarrier is 10.54 μg mL^{-1}, and the ars nanoplatform is 5.11 μg mL^{-1}, which also demonstrates the excellent stability of the nanoplatform (Figure S2E, Supporting Information). Ultraviolet (UV) spectroscopy confirmed that the ARS nanoplatform was successfully coupled with ICG (Figure 1H). Furthermore, good photothermal effects were observed upon near-infrared laser irradiation of the nanoplatform suspension, proving that ICG had been coupled to the nanoplatform surface (Figure S2F,G, Supporting Information). The artesunate content was quantitatively determined by measuring its absorbance at 222 nm, followed by calculation using the pre-established concentration-absorbance calibration curve from previous study.[27] The drug loading capacity of ARS in the nanoparticles reached 12 ± 1%. Finally, Fourier transform infrared (FTIR) analysis of the nanoplatform components revealed that no additional reactions occurred during nanoparticle assembly, as indicated by comparison of the spectral curves (Figure S2H, Supporting Information). Finally, the drug release behavior of the nanoplatform was systematically investigated. The results demonstrated that the nanoplatform released a minimal amount of the drug within the first 24 h, followed by a rapid release phase after 24 h, eventually reaching a steady state at 72 h (Figure S2I, Supporting Information).

After nanoplatform had been successfully prepared, we next evaluated its toxic effects on TNBC cells and CAFs in vitro. The nanoplatform exhibited good in vitro cytotoxicity (Figure S3A, Supporting Information). As previously mentioned, activation of the IL-6/STAT3 signaling axis can lead to tumor fibrosis, reducing the effectiveness of subsequent treatments; thus, the inhibitory effect of the ARS nanoplatform on cellular IL-6

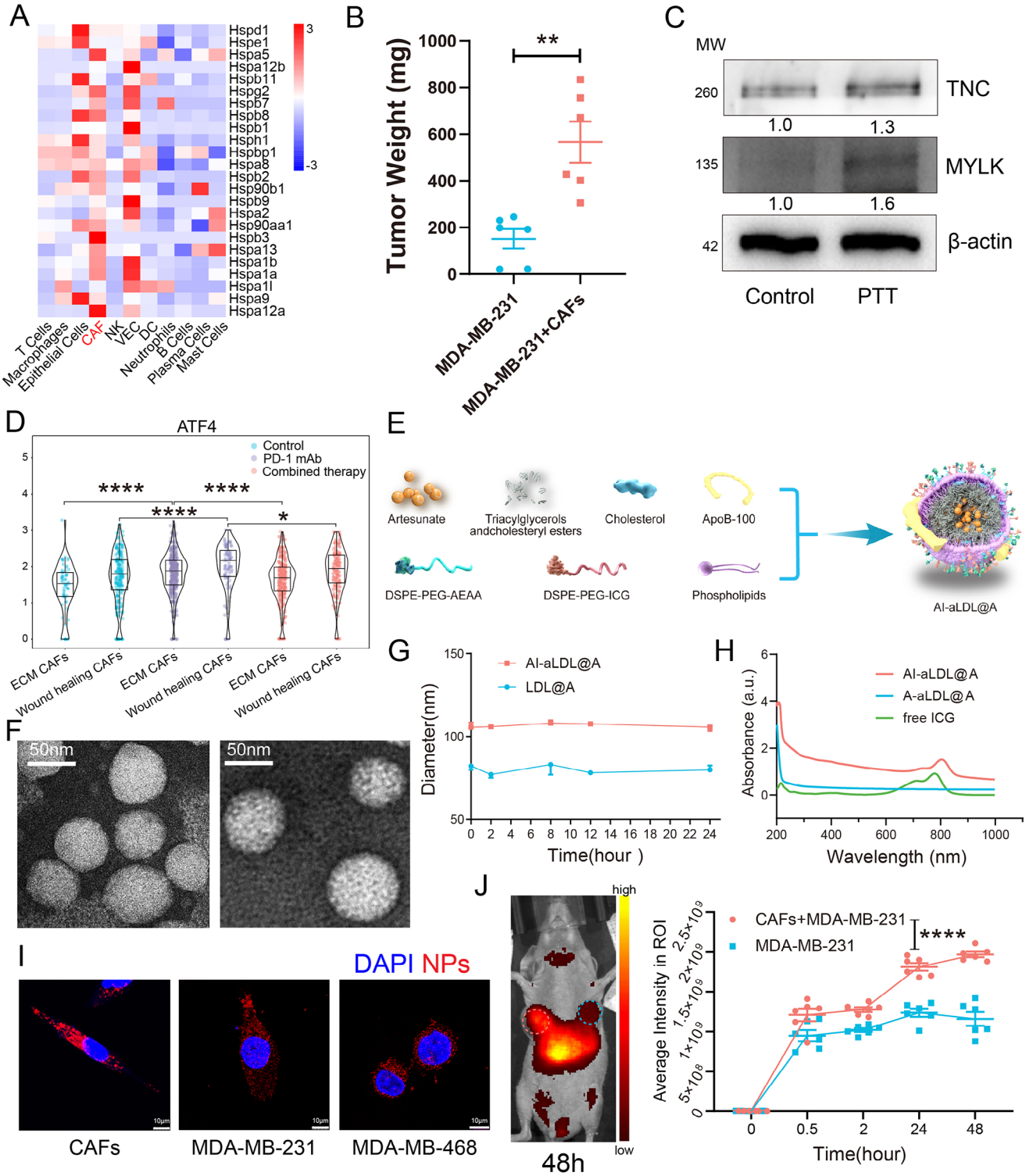

Figure 1. CAFs are involved in PTT resistance and characterization of the artesunate nanoplatform. A) sc-RNA-seq data showing the mRNA expression levels of heat shock proteins in different cell clusters within Eo771 tumors ($n = 6$ independent samples). B) Comparison of tumor weights between the Control group and the Fibrosis group on day 6 after PTT treatment ($n = 6$ independent samples, data expressed as Mean ± S.E.M, statistical comparison using t-test). C) Immunoblotting assessment of ECM CAF marker expression levels in pooled tissue proteins from the control group and tissues treated with free ICG-mediated PTT. D) ATF4 expression in ECM CAFs and wound healing CAFs in the control group, PD-1 mAb group, and combination therapy group (PLGA coated with the ARS nanomedicine and PD-1 mAb combination therapy); statistical comparisons were performed via the Wilcoxon rank-sum test, data are presented as boxplot. E) Schematic of the structure of the dual-targeting artesunate nanoplatform. F) FESEM images of LDL@A

secretion was evaluated. Notably, the nanoplatform reduced the secretion of IL-6 from cells (Figure S3B, Supporting Information), which is consistent with previous reports that ARS blocks the IL-6/STAT3 pathway.[17,45,46] The type of cell death induced by the ARS nanoplatform was further characterized, and the results revealed that this nanoplatform caused mainly cell apoptosis and pyroptosis (Figure S3C, Supporting Information). The inhibitory efficiency of the ARS nanoplatform on CAF cells was further evaluated. Compared with the free state of ARS and ICG, the ARS nanoplatform has demonstrated superior suppression effects (Figure S3D,E, Supporting Information). The in vitro targeting effect of the nanoplatform was also assessed. AI-aLDL demonstrated good in vitro targeting of human CAFs, human breast cancer cells, mouse-derived fibroblasts and TNBC cells (Figure 1I; Figure S4A–C, Supporting Information). Notably, *Sigmar1* expression in ECM CAFs was the highest among all the CAF subtypes evaluated (Figure S4D, Supporting Information). To verify the ability of the nanoplatform to target CAFs in vivo, we further assessed the accumulation of the nanoplatform in human CAF and MDA-MB-231 cell coimplanted tumors and in tumors composed of only TNBC cells (Figure S5A, Supporting Information). The nanoplatform exhibited greater accumulation in the coimplanted tumors (Figure 1J; Figure S5B, Supporting Information). On the other hand, we transiently suppressed sigmar1 expression in tumor tissues using small interfering RNA (siRNA) (Figure S5C, Supporting Information), and observed a significant decrease in the targeting efficacy of the ARS nanoplatform (Figure S5D,E, Supporting Information). This outcome demonstrates that the ARS nanoplatform possesses specific targeting capability toward the sigmar1 receptor. Moreover, 48 h after nanoplatform injection, its accumulation within the viscera was further evaluated, and the results revealed that the nanoparticles accumulated in the liver and kidney (Figure S5F, Supporting Information). Finally, the penetration efficiency of the nanoplatform in highly fibrotic tumors was investigated. The results show that the nanoplatform with AEAA attached exhibits better penetration efficiency compared with the nanoplatform without AEAA connection (Figure S5G,H, Supporting Information).

In summary, we successfully prepared an ARS nanoplatform. The nanoplatform demonstrated good targeting toward CAFs and TNBC tumor models. In vitro, the nanoplatform was shown to mediate PTT-induced tumor cell killing and inhibit cellular IL-6 secretion.

2.3. The ARS Nanoplatform can Sensitize TNBC Cells to ICG-Mediated PTT

Furthermore, we validated the effectiveness of the nanoplatform in various TNBC mouse models (**Figure 2**A; Figure S6A, Supporting Information). First, the ARS nanoplatform demonstrated excellent therapeutic effects in a human TNBC xenograft tumor model (Figure 2B,C; Figure S6B, Supporting Information). As expected, compared with the PTT group (AI-aLDL+L and I-LDL+L), the combination therapy group (AI-aLDL@A+L and I-LDL@A+L) presented better therapeutic effects (Figure S6C, Supporting Information). These results demonstrated specifically inhibiting ECM CAFs could enhance the efficacy of PTT in treating TNBC. Notably, tumor posttraumatic stress can cause drug resistance and fibrosis in tumors, increasing the difficulty of subsequent tumor treatment.[9,47,48] HSP70, Ras, JNK, and RhoA have all been reported to be strongly associated with posttraumatic stress in tumors.[49–52] Notably, the expression of stress-related proteins in the tumor tissues of the combined treatment group was lower than that in the I-LDL+L group (Figure 2D). The result suggested that artesunate could inhibit posttraumatic stress in tumor. Further, the immunohistochemistry results revealed greater JNK expression in the tumor tissue and at the PTT ablation area interface in the I-LDL+L group than in the I-LDL@A+L group (Figure 2E). This phenomenon was also observed in MDA-MB-468 tumors (Figure S6D,E, Supporting Information). Immunohistochemical analysis and quantification confirmed the inhibitory effect of ARS on JNK expression (Figure S7A–C, Supporting Information). Thus, ARS effectively reduced tumor stress after PTT. To further confirm the induction effect of PTT on ECM CAFs, we used C57BL/6J mice to construct an Eo771 mouse TNBC model. The ARS nanoplatform again demonstrated excellent therapeutic effects and significantly inhibited JNK (stress-related protein) expression (Figure 2F,G; Figure S7D, Supporting Information). To directly evaluate the ability to alleviate the occurrence of tumor fibrosis after reducing CAF stress, we performed immunofluorescence. The result revealed an increase in ECM CAFs in tumor tissues after PTT (Figure 2H).Additionally, higher ATF4 expression was detected in the I-LDL+L group than in the control group, indicating that PTT induces tumor stress and fibrosis (Figure 2H,I). However, the detection of inflammation-related factors in mouse blood suggested that the ARS nanoplatform could reduce the degree of tumor fibrosis caused by inflammatory storms after PTT (Figure 2J). To further confirm the specific inhibitory effect of the ARS nanoplatform on ECM CAF. We collected tissues from different groups of mice for immunofluorescence and immunoblotting assessment. The results showed that the expression intensity of TNC and MYLK in the combination group significantly reduced than only PTT group (Figure S7E–G, Supporting Information; Figure 2K). Tumor fibrosis often causes drug resistance,[53,54] developed nanoplatform (AI-aLDL@A) could achieve superior PTT effect after inhibiting ECM CAFs. Therefore, the design strategy of AI-aLDL@A was successful, and the PTT resistance caused by CAF stress can be overcome.

(left) and AI-aLDL@A (right); scale bar: 50 nm. G) Hydrated sizes of LDL@A and AI-aLDL@A at different time points (0, 2, 8, 12, and 24 h) ($n = 3$ independent experiments; data are expressed as the mean ± S.E.M. values). H) UV absorbance spectra of AI-aLDL@A, A-aLDL@A, and free ICG. I) The targeting of AI-aLDL (red) to CAFs and TNBC cells (blue) was assessed via laser confocal microscopy; scale bar: 10 μm. J) Representative fluorescence images of a mouse within 48 h after intravenous injection (red circle: coimplanted CAFs and MDA-MB-231 cells; blue circle: MDA-MB-231 cells only) and quantification of the fluorescence intensities in the tumors on both sides at different time points ($n = 6$ independent samples; data are expressed as the mean ± S.E.M. values; statistical comparisons of the quantified data at the 48 h time point were performed via Student's t test). Some data (A, D) were reanalyzed on the basis of our previously published data. * $p < 0.05$, **** $p < 0.0001$.

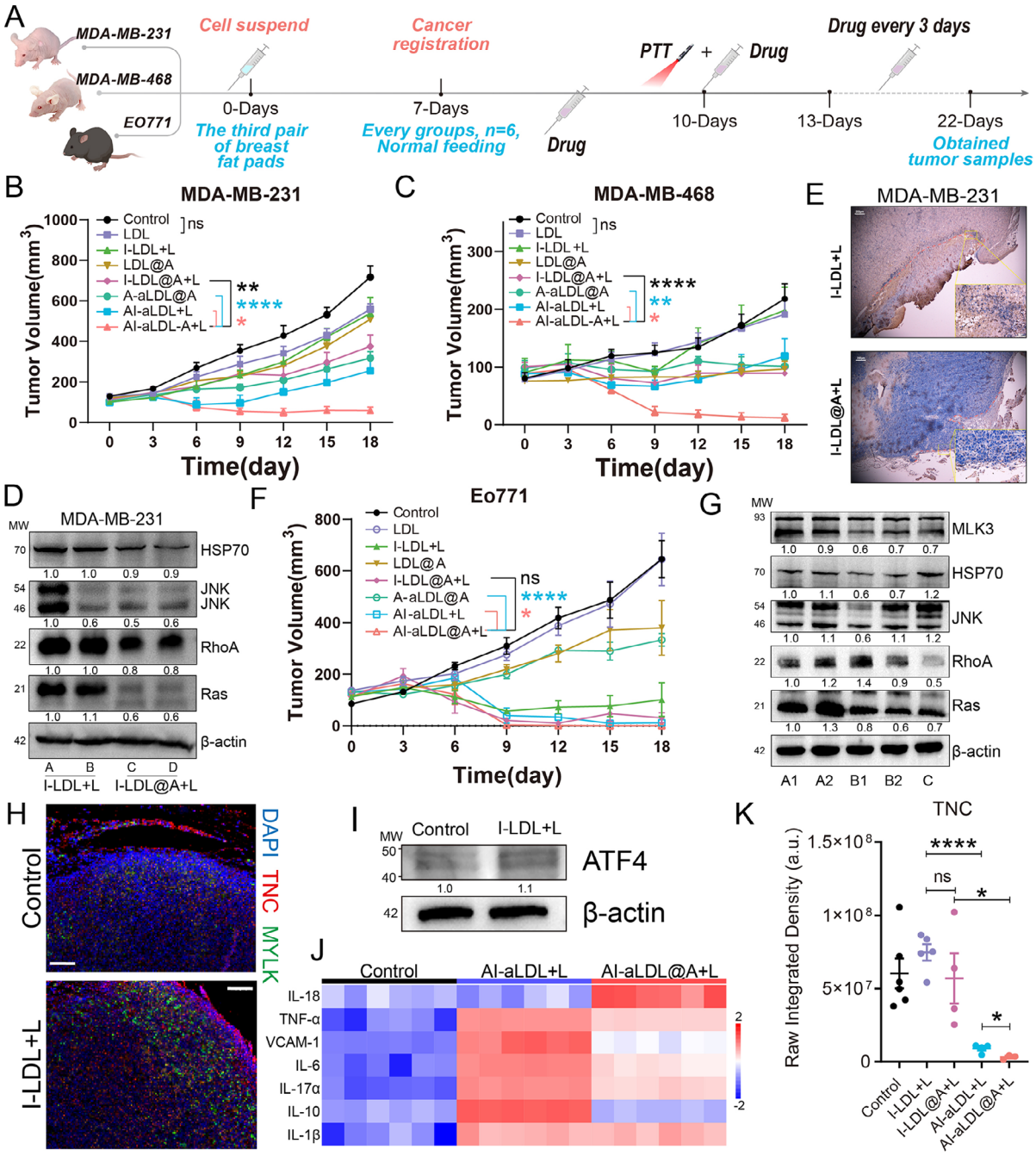

Figure 2. The artesunate nanoplatform alleviates stress after PTT in multiple TNBC models. A) Schematic of the in vivo experiments with the nanomedicine. B,C) Tumor response curves in MDA-MB-231 and MDA-MB-468 xenograft models after treatment with the nanomedicine ($n = 6$ independent samples; statistical comparisons of tumor volume on the 18th day were performed via Student's t test). D) Expression of HSP70, JNK, RhoA, and Ras in the tumor tissues of the mice in the I-LDL+L and I-LDL@A+L groups. E) Immunohistochemical images of mouse tumor tissues expressing JNK; red dashed lines indicate the interface between the ablation area and tumor tissue; scale bars: 200 μm (low magnification) and 50 μm (high magnification). F) Tumor response curves from the Eo771 mouse tumor model after treatment with the nanomedicine ($n = 6$ independent samples; statistical comparisons of tumor volume on the 18th day were performed via Student's t test). G) Expression of stress-related proteins within mouse tumor tissue in different groups (A: control, B: A-aLDL@A, and C: I-LDL@A+L). H) Representative immunofluorescence images of the TNC (green) and MYLK (red) expression distribution in tumor tissues (blue); scale bar: 100 μm. I) Immunoblotting of ATF4 expression in pooled tissue proteins from all the mice in the control group and the I-LDL+L group. J) Concentrations of inflammatory cytokines in the serum of mice in different groups after treatment ($n =$ 6 independent samples). K) The immunofluorescence intensity quantification results of TNC for each Eo771 tumor in different groups (control n = 6, I-LDL+L n = 6, I-LDL@A+L n = 4, AI-aLDL+L n = 4, AI-aLDL@A+L n = 3), statistical comparisons were performed via Student's t test. Groups that received laser irradiation treatment are indicated by +L. The data in (B,C,F,K) are expressed as the mean ± S.E.M. values.* $p < 0.05$, ** $p < 0.01$, **** $p < 0.0001$, ns no significance.

We further compared the heating effects mediated by the targeted nanoplatform and the nontargeted nanoplatform in vivo to evaluate the targeting efficacy of the nanoplatform. The ARS nanoplatforms (AI-aLDL and AI-aLDL@A) exhibited superior PTT effects (Figure S8A–C, Supporting Information). Importantly, targeted drug delivery can reduce in vivo side effects. Therefore, we also assessed the in vivo toxicity of the ARS nanoplatform. Macroscopically, the nanoplatform did not significantly reduce the body weight of the mice at the end of the treatment cycle (Figure S9A, Supporting Information). Given that the nanoplatform accumulated in the liver and kidney, the effects of the nanoplatform on liver and kidney function were further evaluated. A detailed evaluation revealed that the ARS nanoplatform caused less liver and kidney function damage trend (Figure S9B, Supporting Information), and hematoxylin and eosin (H&E) staining of liver and kidney tissues also indicated that the nanoplatform did not have significant toxic effects (Figure S9C, Supporting Information). The biosafety profile of ARS nanoplatform is fundamentally ensured by its exclusively clinical-grade components, all possessing well-established biocompatibility in human applications. Importantly, no significant body weight reduction was observed even in non-targeting group mice (Figure S9A, Supporting Information). ARS nanoplatform demonstrates further reduced toxicity (Figure S9B, Supporting Information). Comprehensive biosafety assessments (including histopathological evaluation of major organs and serum biochemical parameters) consistently confirmed the outstanding biocompatibility profile of nanoplatform.

In summary, the ARS nanoplatform achieved excellent therapeutic effects in multiple TNBC mouse models after a single laser irradiation. This effectiveness is attributed to ability of the nanoplatform to target CAFs and cancer cells and its specific inhibition of CAFs, which result in better PTT effects. Moreover, the ARS nanoplatform has good biosafety.

2.4. Spatial Transcriptomics Confirmed that the Tissue Resistance Barrier Formed by ECM CAFs was Involved in PTT Resistance

The above results highlight the importance of CAFs, especially ECM CAFs, in PTT resistance. We used spatial transcriptomics to analyze the impact of the spatial distribution of ECM CAFs within tumor tissues on PTT efficacy. To evaluate the contribution of inefficient PTT to tumor heat resistance. We selected tumors from the non-targeted groups (I-LDL+Laser and I-LDL@A+Laser), as well as tumors from the control and A-aLDL@A groups, for spatial transcriptome sequencing analysis.

On the basis of gene expression profiles, we predicted the spatial distributions of various cell clusters within tumor tissues. In the I-LDL+L group, the tumor margins presented high expression of CAFs and macrophage-related markers, indicating their colocalization (**Figure 3**A). This is similar to the previously reported immune barrier formed by CAFs and tumor-associated macrophages (TAMs).[55] In contrast, the tissue resistance barrier formed in the combination therapy group (I-LDL@A+L) was significantly reduced (Figure 3A). Moreover, the negative control groups (the control group and the A-aLDL@A group) did not present typical tissue barrier structures (Figure S10A, Supporting Information). Given that it is still unknown which specific subtypes of CAFs and TAMs form this tissue resistance barrier, we performed further investigations. On the basis of previous reports that *Spp1* is a major marker of such tissue barrier cells,[56,57] we analyzed the interaction intensities of macrophages and various fibroblast subtypes in the SPP1 pathway. As expected, M2 macrophages strongly interacted with ECM CAFs and wound healing CAFs via the SPP1 pathway (Figure 3B). Furthermore, we defined eight subtypes of macrophages. First, we performed GOBP analysis on the basis of the gene expression profiles of each macrophage subtype to preliminarily determine the main enriched pathways in each subtype (Figure S10B, Supporting Information). More importantly, we referred to the primary macrophage markers defined in the published literature and analyzed the expression of these markers in different macrophage subtypes to define the eight macrophage subtypes[58–61] (Figure S10C,D, Supporting Information).

Subsequent analysis via scRNA-seq revealed strong interactions between ECM CAFs, wound healing CAFs, and plasma-like macrophages (Figure 3C). To confirm the spatial localization between ECM CAFs, wound healing CAFs, and plasma-like macrophages, spatial transcriptomics mapping was performed. The results revealed that plasma-like macrophages and ECM CAFs were colocalized (Figure 3D). Spot deconvolution analysis also confirmed the colocalization relationship between ECM CAFs and plasma-like macrophages (Figure S11A, Supporting Information). Based on the clustering logic in scRNA-seq, where *Col1a1* serves as the primary identifier for CAFs, we first preliminarily localized CAF spatial distribution within tumors using Col1a1. Furthermore, to provide more objective validation of our results, we employed the well-established CAF marker α-SMA for secondary spatial mapping. Finally, co-localization of TNC with α-SMA and COL1A1 was performed. Notably, results from multiplex immunofluorescence staining of tissue specimens further validated the capability of spatial transcriptomic sequencing in accurately mapping the anatomical distribution of ECM CAFs (Figure S11B,C, Supporting Information). Wound healing CAFs colocalized with ECM-associated macrophages (Figure S12A, Supporting Information). These results suggested that this tissue resistance barrier is composed primarily of ECM CAFs and plasma-like macrophages rather than wound-healing CAFs. The multi-immunofluorescence and marker coexpression results further supported the above findings (Figure 3E,F). In the I-LDL@A+L group, the *Atf4* expression levels tended to decrease within the area close to blood vessels (0–40), whereas those in the I-LDL+L group did not significantly change (Figure 3G). It reflected that artesunate could inhibit tumor stress to avoiding fibrosis. Considering that ARS can inhibit the IL-6/STAT3 pathway,[45,46] we next evaluated the interaction between ECM CAFs and various macrophage subtypes in terms of the IL-6 signaling pathway and found interactions between ECM CAFs and plasma-like macrophages in this pathway (Figure 3H). Quantification of the proportion of ECM CAF and plasma-like macrophages within different samples also showed the inhibitory effect of ARS on ECM CAFs (Figure S12B, Supporting Information). Therefore, the ARS nanoplatform specifically inhibits the interaction between ECM CAFs and plasma-like macrophages, thereby reducing the formation of a tissue resistance barrier. To further directly confirm the inhibitory effect of

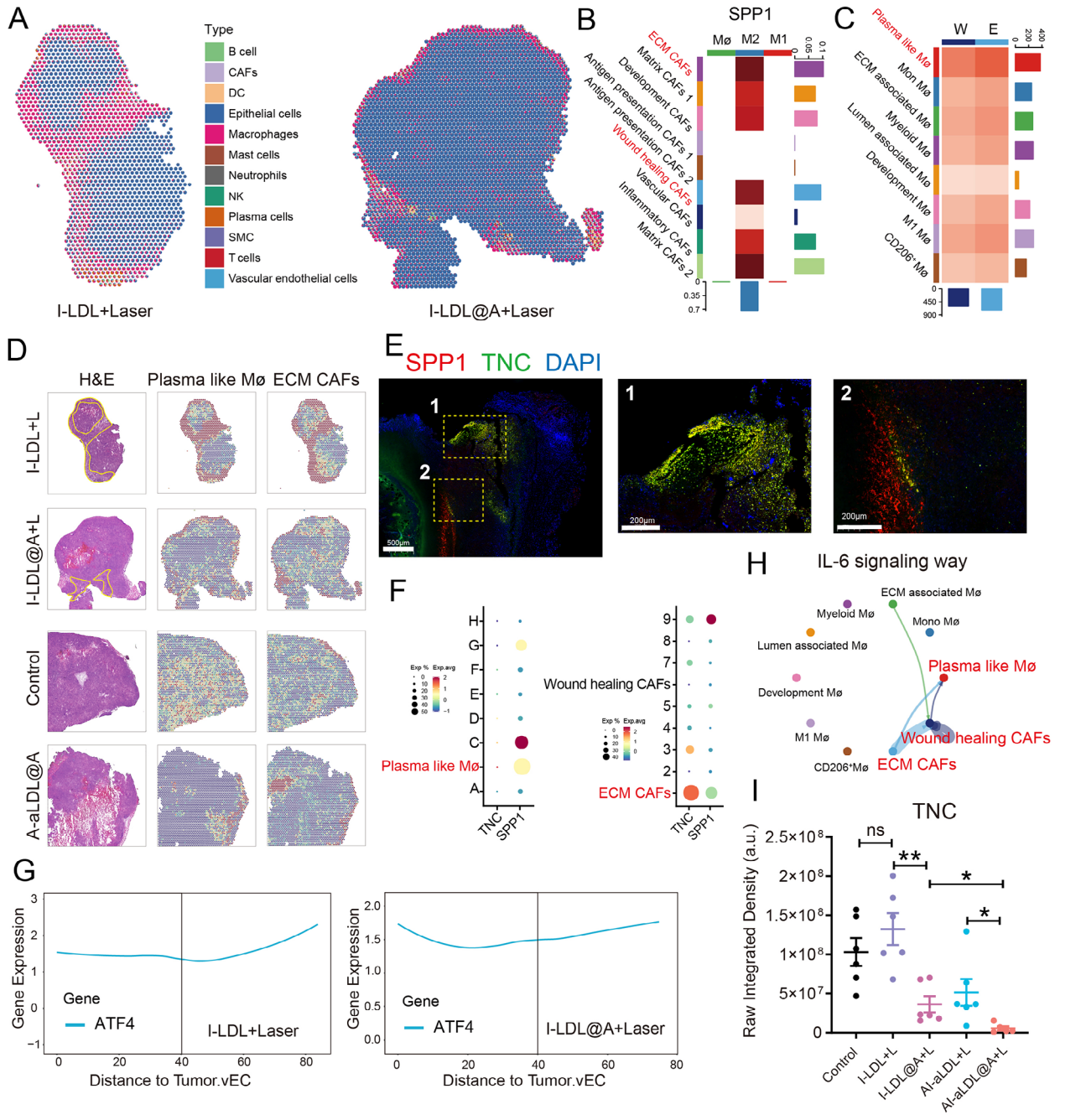

Figure 3. Spatial transcriptomics confirmed that the tissue resistance barrier composed of ECM CAFs participated in PTT resistance. A) Gene expression at each dot was used to predict the spatial distribution of different cell types and perform space mapping ($n = 1$/ group). B) Interaction strength between different CAF subtypes and macrophages in the SPP1 signaling pathway. C) Interaction strength between E (ECM CAFs), W (wound healing CAFs) and various TAM subtypes; clusters of interest are marked in red. D) H&E staining images of tumor tissues from different groups and spatial distribution prediction of ECM CAFs and plasma-like macrophages in tumor tissue on the basis of the expression of the top gene at each site; the yellow line indicates fibrous H&E-stained tissue. E) Multi-immunofluorescence evaluation of the SPP1 (red) and TNC (green) distribution in tumor tissue from I-LDL+Laser group; scale bars: 500 μm (low magnification) and 200 μm (high magnification). F) Dot plot of TNC and SPP1 expression in different macrophage subtypes (A: mononuclear MØ; C: ECM-associated MØ; D: development MØ; E: myeloid MØ; F: M1 MØ; G: lumen-associated MØ; and H: CD206$^+$ MØ) and CAF subtypes (2: matrix CAFs 1; 3: development CAFs; 4: antigen-presenting CAFs 1; 5: antigen-presenting CAFs 2; 7: vascular CAFs; 8: inflammatory CAFs; and 9: matrix CAFs 2). G) Relationships between the expression levels of the ATF4 genes and the distance from the selected tumor vascular region, with distances ranging from 0 to 40 for the main comparison area. H) Strengths of the interactions between ECM CAFs, wound healing CAFs, and various TAM subtypes in the IL-6 signaling pathway; the clusters of interest are marked in red. I) The immunofluorescence intensity quantification results of TNC for each MDA-MB-231 tumor in different groups ($n = 6$ independent samples per group, AI-aLDL@A+L n = 5), statistical comparisons were performed via Student's t test. Groups that received laser irradiation treatment (D,I) are indicated by +L.* $p < 0.05$, ** $p < 0.01$, ns no significance.

ARS on ECM CAFs, we evaluated TNC and MYLK expression levels in tumor tissues of MDA-MB-231. The results also showed that the expression intensity of TNC and MYLK in the combination group significantly reduced than only PTT group (Figure S12C,D, Supporting Information; Figure 3I). These results also implied the inhibitory effect of the ARS nanoplatform on ECM CAF.

In summary, the ARS nanoplatform can specifically weaken the tissue barrier composed of ECM CAFs and plasma-like macrophages.

2.5. Serine Metabolism is More Active in ECM CAFs

ATF4 is an important marker of stress in CAFs that also regulates the expression of key enzymes involved in intracellular serine synthesis.[62,63] Therefore, we further explored whether serine metabolism could be a potential target for ECM CAF inhibition. On the basis of the expression of genes in each CAF subtype, we predicted their enrichment in metabolic pathways. ECM CAFs were highly enriched in amino sugar and nucleotide sugar metabolism, the TCA cycle, and the pentose phosphate pathway (**Figure 4A**). Of note, serine depletion can inhibit tumor nucleotide metabolism and energy synthesis.[64–67] Therefore, we mapped the spatial distribution of nucleotide-related metabolites in tumors. Compared with those in the control group, the abundances of uridine 5′-monophosphate, guanosine monophosphate, and uridine were lower in the A-aLDL@A group (Figure 4B). Furthermore, uridine 5′-monophosphate, methacholine, and citric acid were more abundantly expressed in ECM CAFs than in other tumor regions (Figure 4C; Figure S13A, Supporting Information). Notably, methacholine, as a one-carbon unit, is involved in the interconversion between serine and glycine. As expected, metabolic enrichment analysis revealed that ECM CAFs are highly active in the glycine, serine and threonine metabolism pathway (Figure 4D). Therefore, the serine metabolism pathway is a potential metabolic target of ECM CAFs.

Given the colocalization of ECM CAFs and plasma-like macrophages, we first compared the metabolic pseudotime distributions of both to confirm the specificity of serine metabolism in ECM CAFs and found that they presented similar metabolic distributions (Figure 4E). However, when the distributions of choline, thymine, phenylacetylglycine and creatine in ECM CAFs and plasma-like macrophages were compared, these compounds were significantly more abundant in ECM CAFs than in plasma-like macrophages (Figure 4F; Figure S13B, Supporting Information). These findings support the conclusion that the serine metabolism pathway is highly active in ECM CAFs. Similarly, pathway enrichment on the basis of the metabolic abundance of tumor tissues from the control group and the A-aLDL@A group revealed significant regulation of the serine metabolism pathway and the choline pathway in the A-aLDL@A group (Figure 4G). Further, the ARS nanoplatform can specially target ECM CAFs due to the higher expression of sigmar1 in ECM CAFs than macrophages (Figure S4D, Supporting Information). Therefore, the ARS nanoplatform could inhibit glycine/serine/threonine metabolism pathway in ECM CAFs.

Overall, the serine pathway is a potential metabolic target for ECM CAFs, and the ARS nanoplatform can reduce the abundance of metabolites related to the serine pathway, thus specifically inhibiting ECM CAFs.

2.6. The ARS Nanoplatform Inhibits the MAPK Cascade and Serine Homeostasis in CAFs

To elucidate the mechanism by which the ARS nanoplatform inhibits the ability of CAFs to reverse PTT resistance (**Figure 5A**), tumor tissues from the control and ARS-targeted delivery groups (A-aLDL@A) were subjected to transcriptomic sequencing (RNA-seq), proteomics, and metabolomics analyses (Figure S14A, Supporting Information). Considering that temperature change during PTT therapy can induce MAPK pathway activation.[68] we first evaluated the expression of different CAF subtypes in the MAPK pathway. The level of MAPK cascade was significantly higher in ECM CAFs than in the other subtypes (Figure 5B). RNA-seq and proteomics revealed that MAPK pathway-related genes were inhibited upon treatment with the ARS nanoplatform (Figure S14A, Supporting Information). Given the important roles of proteins in cellular functions, we further performed enrichment analysis of the proteins whose expression were reduced in the A-aLDL@A group. The enrichment results indicated that the ARS nanoplatform significantly inhibited the tumor MAPK cascade (Figure 5C), and as expected, metabolomics revealed significant inhibition of one-carbon units (Figure S14A, Supporting Information). Therefore, the ARS nanoplatform can specially inhibit MAPK cascade and serine metabolism in ECM CAFs.

To further explore the regulatory relationship between serine metabolism and the MAPK pathway cascade in CAFs, we examined how serine depletion affects MAPK pathway-related genes at both the protein and transcription levels. Interestingly, these genes presented opposite trends at the protein and transcription levels (Figure 5D,E; Figure S14B, Supporting Information). These markers exhibited a decreasing then increasing trend at the protein level and an increasing then decreasing trend at the transcription level. Moreover, after reanalysis, the RNA-seq and proteomics data revealed that these markers exhibited similar trends (Figure S14C,D, Supporting Information). Furthermore, the nuclear transcription factors driving CAF differentiation were also inhibited by serine depletion (Figure S14E, Supporting Information), and these nuclear transcription factors showed similar trends at both the protein and transcription levels (Figure S14E,F, Supporting Information). To confirm the specificity of serine depletion in CAF inhibition in breast cancer, human TNBC cells and mouse TNBC cells were also subjected to serine depletion, and this phenomenon was not observed (Figure S15A-D, Supporting Information).

Overall, serine depletion affects the MAPK pathway cascade in CAF cell, but their specific regulatory relationship remains still unclear.

2.7. Serine Depletion Affects GTPase Activity in CAFs

Given that the regulatory relationship between serine homeostasis and the MAPK cascade in CAFs is not yet clear, the regulatory mechanisms involved were further explored to identify

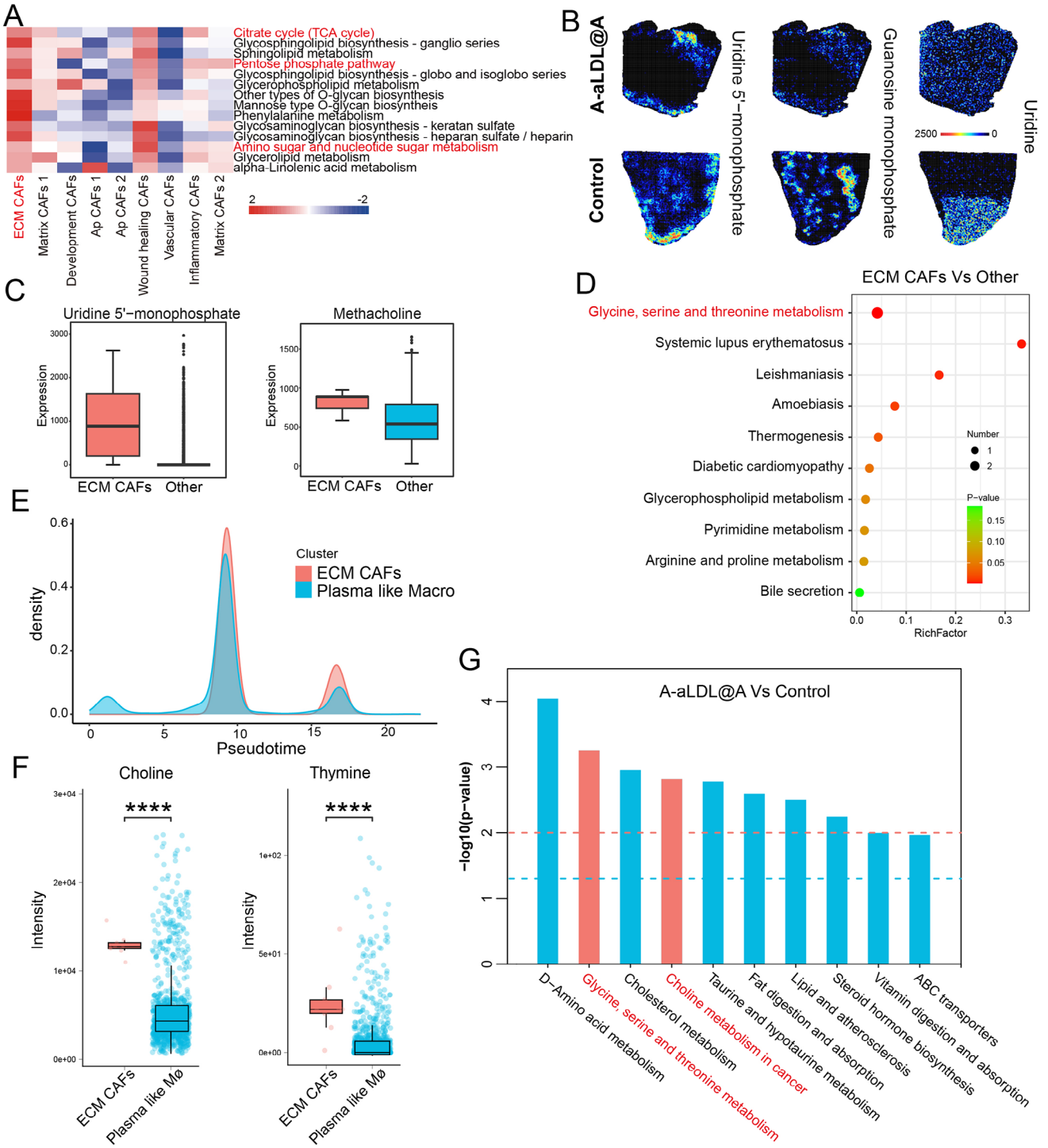

Figure 4. ECM CAFs are highly correlated with serine metabolism. A) Prediction of the expression levels of various CAF subtypes in different metabolic pathways on the basis of gene expression from scRNA-seq; the cluster and pathways of interest are marked in red. B) Spatial mapping of representative metabolite (nucleotide) expression in tumor tissue from the control and A-aLDL@A groups. C) Comparison of the levels of uridine 5′-monophosphate (pyrimidine nucleotide) and choline (one-carbon unit) expression in ECM CAF regions and other regions, data are presented as boxplot. D) Enrichment of metabolic pathways on the basis of metabolite expression in ECM CAF regions and other regions; the pathways of interest are marked in red. E) Pseudotemporal analysis of the metabolite intensity distribution in ECM CAFs and plasma-like macrophages. F) Comparison of the expression levels of choline, thymidine, and metabolites in ECM CAFs and plasma-like macrophages. Data are presented as boxplot. Statistical comparisons were performed via Student's *t*-test. G) Top 10 enriched metabolic pathways on the basis of the expression of all metabolites in the control and A-aLDL@A groups; the pathways of interest are marked in red. **** $p < 0.0001$.

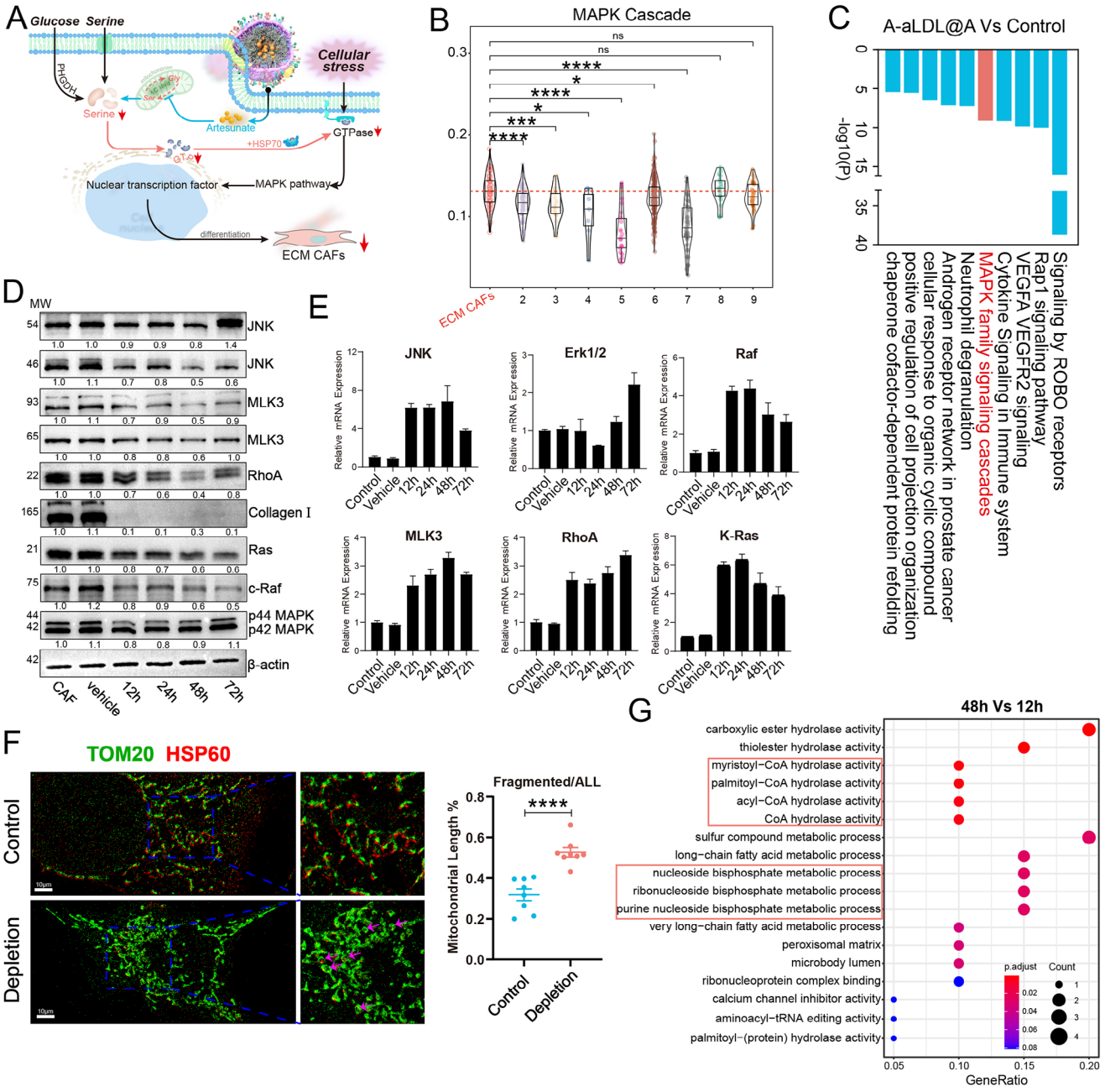

Figure 5. Mechanism of serine regulation of the MAPK pathway in CAFs. A) Schematic representation of the regulatory mechanism of the artesunate nanoplatform in CAFs. B) Signature score analysis in pathway (MAPK cascade) on the basis of gene expression in different CAF subtypes (2: matrix CAFs 1; 3: development CAFs; 4: antigen-presenting CAFs 1; 5: antigen-presenting CAFs 2; 6: wound healing CAFs; 7: vascular CAFs; 8: inflammatory CAFs; and 9: matrix CAFs 2); the subtypes of interest are marked in red, and the red dashed line indicates the median value of ECM CAFs, which was used as a reference; statistical comparisons were performed via the Wilcoxon rank-sum test. Data are presented as boxplot. C) Pathway (Top10) enrichment based on differential proteins (A-aLDL@A Vs Control, Top100 in down-regulated proteins) through Metascape, focus pathway marked in red. D) Expression of MAPK pathway-related proteins in CAFs after serine depletion for different durations. E) Transcriptional expression of MAPK pathway-related genes in CAFs after serine depletion for different durations ($n = 3$ independent samples; data are expressed as the means ± S.E.M. values). F) Ultrahigh-resolution laser confocal microscopy evaluation of changes in mitochondrial morphology (TOM20: green; and HSP60: red) in CAFs after 48 h of serine depletion and quantitative analysis; scale bar: 10 μm ($n = 8$ independent samples; data are expressed as the mean ± S.E.M. values; statistical comparisons were performed via Student's *t*-test). G) GO pathway enrichment of the differential proteins (significant differences) with ^{13}C-labeled serine in CAFs between 12 and 48 h; the pathways of interest are indicated in the red boxes.* $p < 0.05$, *** $p < 0.001$, **** $p < 0.0001$, ns no significance.

new targets for PTT sensitization. Serine depletion caused opposing trends in MAPK pathway-related genes at the protein and transcription levels, potentially due to blockade of posttranslational modification processes, which led to compensatory increases in transcription levels. The Golgi apparatus, endoplasmic reticulum, and mitochondria are the main cellular sites at which posttranslational modifications occur. Given that the mitochondria are the sites at which serine and glycine interconversion occurs via one-carbon units,[64,67] we evaluated the impact of serine depletion on mitochondria. Serine depletion significantly affected mitochondrial function (Figure 5F; Figure S16A, Supporting Information); moreover, serine was also confirmed to accumulate in the mitochondria (Figure S16B,C, Supporting Information). As expected, JC-1 staining also confirmed that serine depletion reduced the mitochondrial membrane potential level and affected mitochondrial function in CAF cells (Figure S16D, Supporting Information). We further assessed the role of serine in the mitochondria using ^{13}C-labeled serine for metabolic tracing. Upon serine depletion, the isotopically labeled serine was replenished for 12 and 48 h. The ^{13}C-labeled proteins were categorized into two types: those where all serine sites in the peptide segment were labeled with ^{13}C and those where only some serine sites were labeled with ^{13}C. The comparisons of the differentially expressed proteins and all proteins labled with ^{13}C were performed. The results showed that serine was closed to nucleotide metabolism, CoA activity pathways and GTPases activity (Figure 5G; Figure S16E, Supporting Information). Therefore, serine depletion interferes with energy metabolism and further inhibits GTPase activity of MAPK pathway in CAFs.

Interestingly, we found that the proteins involved in the response to heat and protein folding among all the differentially expressed proteins were associated mainly with HSP70 (**Figure 6**A). Among them, the DNAJ homolog subfamily of proteins stabilize the ATPase and GTPase activities of HSP70.[69–71] Additionally, HSP70 is an essential intracellular GTP transport carrier.[72–74] Therefore, we hypothesized that serine depletion might affect the HSP70 supply of GTP to GTPases in the MAPK pathway. To verify this hypothesis, we first assessed the distribution of HSP70 in cells before and after serine depletion. As expected, under normal conditions, HSP70 was distributed primarily on the cell membrane; however, after serine depletion, it was distributed mainly around the nucleus (Figure 6B; Figure S16F, Supporting Information). Next, we evaluated the proteins that interact with HSP70. The results revealed that HSP70 interacts with Ras and RhoA (Figure 6C), both of which are receptor-related kinases on the cell membrane.[75–77] Finally, we ruled out the possibility that NCT-503 (a PHGDH inhibitor that inhibits the de novo synthesis pathway of serine)[78,79] itself affects the MAPK pathway (Figure 6D). Serine depletion affects nucleotide metabolism.[80] which disrupts intracellular GTP homeostasis and triggers endoplasmic reticulum stress.[81] This leads to the transfer of HSP70 from the cell membrane location to the nuclear location to help protein folding to maintain the basic survival of the cell. Further, We also observed the same phenomenon caused by serine depletion in mouse fibroblast cell line L929 (Figure 6E,F; Figure S17A,B, Supporting Information). Finally, we inhibited MAP2K7 and HSP70 respectively to further evaluate the regulatory relationship between serine and the cascade activity of MAPK pathway. Inhibition of both MAP2K7 and HSP70 has an impact on the cell stress regulation and cell cycle-related pathways of fibroblasts. However, none of these changes affected the serine metabolism level of the cells (Figure S18A-D, Supporting Information). However, serine depletion can affect the cascade activity of the MAPK pathway. Of note, we had also confirmed the sensitizing effect of serine depletion on PTT both in vitro and in vivo (Figure S18E–G, Supporting Information). These results strengthen our conclusion.

Overall, the ARS nanoplatform can specifically inhibit one-carbon units in CAFs and disrupt serine homeostasis to thereby inhibit intracellular energy synthesis and HSP70 synthesis. A lack of GTP supply to cell membrane receptor-related GTPases reduces the responsiveness of cells to external stimuli. ECM CAFs are especially highly enriched in MAPK cascade, and higher expression of sigmar1, which making them particularly susceptible to inhibition by the ARS nanoplatform.

2.8. MAP2K7 can be Used as a New Target for PTT Sensitization

Interestingly, we found that in the proteins where all of the serine sites were isotope labeled, MAP2K7 plays a role in MAP kinase activity and has corresponding functions in response to heat (Figure 6A,G). Additionally, MAP2K7 expression was increased in mouse Eo771 tumor tissues upon PTT with free ICG (Figure 6H). Therefore, we speculate that MAP2K7 could serve as a new target to sensitize cells to PTT. To further verify the role of MAP2K7 in PTT, we used DTP3, an inhibitor of MKK7. The results showed that PTT combined with DTP3 could produce better therapeutic effects (**Figure 7**A,B).

2.9. Validation Based on CAFs^{HR}

To further validate our previous conclusions, we established in vitro heat-resistant CAFs (CAFs^{HR}) (Figure 7C,D). In PTT experiments incorporating the nanoplatform without ARS, CAFs^{HR} exhibited significant heat tolerance (Figure 7E; Figure S19A, Supporting Information). However, the ARS nanoplatform still inhibited CAFs^{HR} (Figure S19A, Supporting Information). Additionally, the damage repair ability of CAFs^{HR} was assessed, and a significant increase was found (Figure 7F; Figure S19B, Supporting Information). The proliferation rate and inflammatory factor secretion by CAFs^{HR} also significantly increased (Figure 7G; Figure S19C, Supporting Information). Interestingly, when we compared the changes in TNC and MYLK expression between CAFs^{HR} and CAFs, we detected TNC and MYLK increased in CAFs^{HR} (Figure 7H; Figure S19D, Supporting Information), suggesting that PTT can induce the differentiation of CAFs into ECM CAFs. Therefore, we evaluated the protein expression profiles of CAFs^{HR} and CAFs to verify the role of MAP2K7 in promoting heat resistance in CAFs and the effects of PTT on activating the MAPK pathway and increasing serine metabolism in CAFs.

As expected, MAP2K7 expression was significantly increased in CAFs^{HR} (Figure 7I). Compared with CAFs, the collagen-containing ECM and integrin binding pathways of CAFs^{HR} are more enriched (Figure S19E, Supporting Information). Moreover, after ARS nanoplatform-mediated PTT of CAFs^{HR}, we extracted the cell supernatant. Multiplex detection revealed that

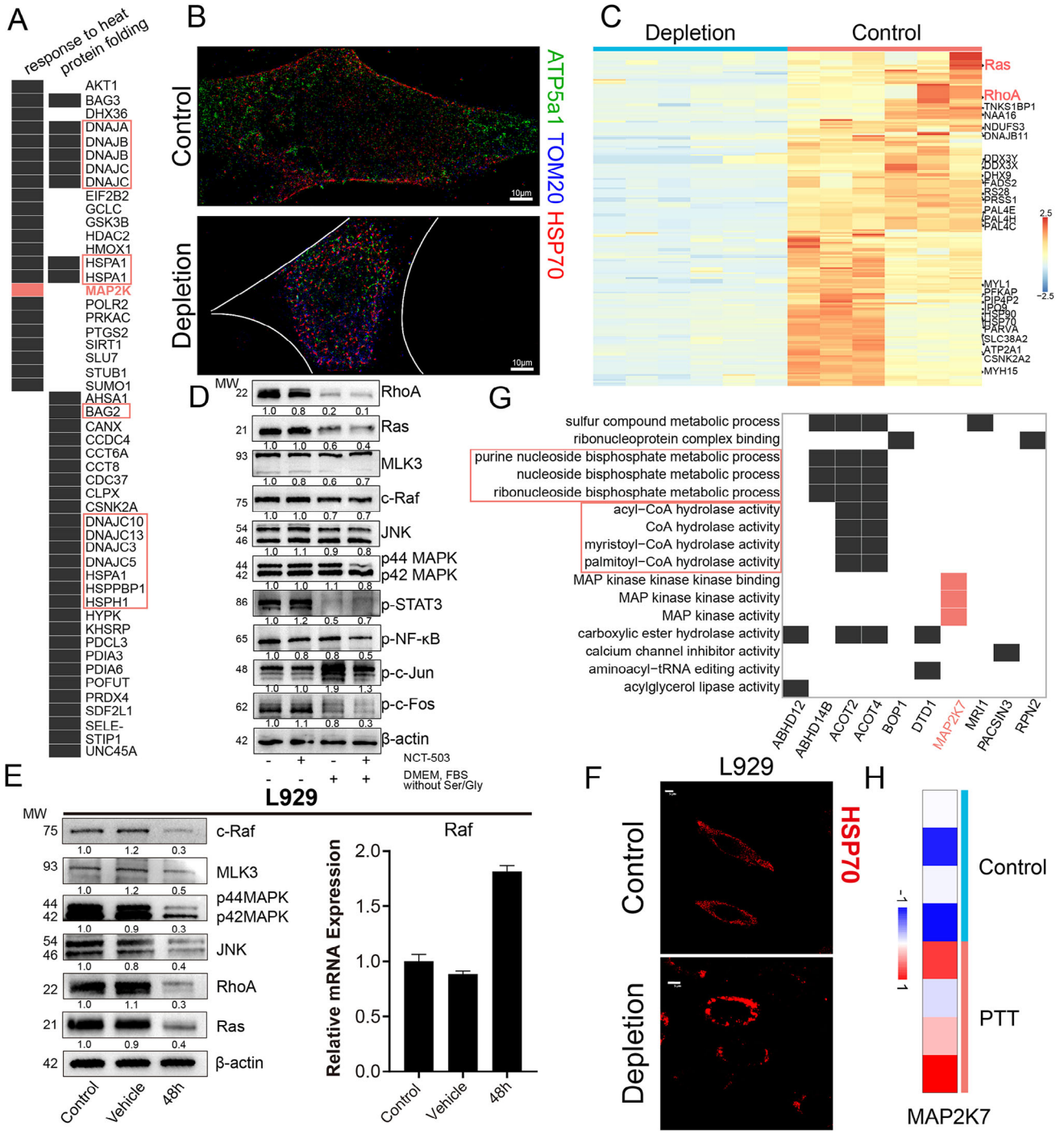

Figure 6. HSP70 plays a role in serine regulation of the MAPK pathway. A) Differential proteins (48 h vs 12 h) with ^{13}C-labeled serine that have protein folding and heat response functions are shown; proteins related to HSP70 are marked in red boxes, and key highlighted proteins are marked in red. B) Ultrahigh-resolution confocal microscopy assessment of the effects of serine depletion on the distribution of HSP70 (red), TOM20 (blue), and ATP5a1 (green) in CAFs (top: HSP70 is distributed along the cell membrane; bottom: white lines indicating cell edges; scale bar: 10 μm). C) Mass spectrometry analysis of proteins after immunoprecipitation was performed to evaluate changes in expression of the proteins that interact with HSP70 in CAFs between the control and serine depletion groups after 48 h. The proteins with the most significant changes in expression and those most related to energy metabolism are noted, with key highlighted proteins shown in red ($n = 6$ independent samples). D) Immunoblot assessment of the inhibitory effects of different serine sources on MAPK pathway-related proteins in CAFs. E) Immunoblotting and qPCR ($n = 3$ independent samples) results were validated in L929 fibroblast cell line with serine depletion for 48 h which affecting on MAPK-related gene. F) Laser confocal microscopy results were validated in L929 fibroblast cell line with serine depletion for 48 h which affecting on HSP70 distribution, scale bar:5 μm. G) GO enriched pathways of the proteins with all the serine sites marked with ^{13}C among the identified peptides; the pathways of interest are marked in red boxes. H) The expression of MAP2K7 in Eo771 tumor from the PTT and control groups ($n = 4$ independent samples).

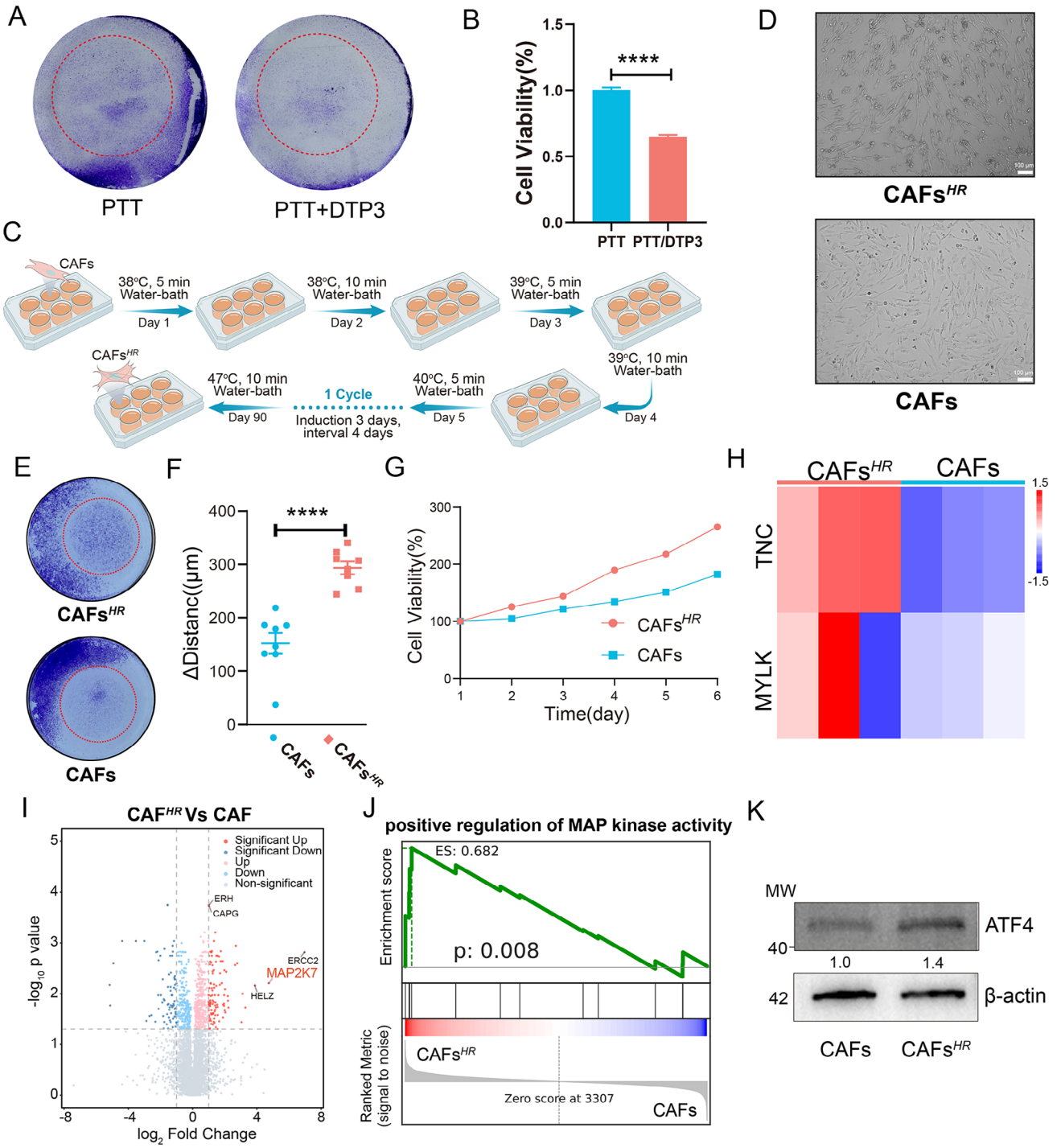

Figure 7. Heat-resistant CAFs were used for validation. A) Crystal violet staining was used to evaluate the killing effects of PTT alone and the MKK7 inhibitor (DTP3) combined with PTT in CAFs; the red dotted line indicates the laser area, and the PTT group was used as a control. B) CCK-8 assays were used to evaluate the killing effects of PTT alone and the MKK7 inhibitor (DTP3) combined with PTT in CAFs; the PTT group was used as a control ($n = 4$ independent samples; statistical comparisons were performed via Student's t test). C) Schematic of the in vitro induction of CAFs^{HR}. D) Cellular morphological characteristics of CAFs and CAFs^{HR} under an optical microscope; scale bar: 100 μm. E) Crystal violet staining of CAFs 96 h after PTT; the laser irradiation area is marked by a red dashed line. F) Comparison of the migration abilities of CAFs and CAFs^{HR} over 96 h ($n = 8$ independent samples; statistical comparisons were performed via Student's t test). G) Growth curves of CAFs and CAFs^{HR} over 6 days ($n = 4$ independent samples). H) Heatmap of TNC and MYLK expression in CAFs and CAFs^{HR}. I) Volcano plot showing differences in protein expression between CAFs and CAFs^{HR} ($n = 3$ independent samples). J) GSEA was performed on the basis of the protein profiles of CAFs and CAFs^{HR}. K) Immunoblotting was used to assess the expression of ATF4 in CAFs and CAFs^{HR}. The data (B,F,G) are expressed as the mean ± S.E.M. values. **** $p < 0.0001$.

CAFs^{HR} secreted more EGF (Figure S20A, Supporting Information), which, as the main ligand for EGFR, can activate downstream pathways such as the MAPK pathway.[82] Similarly, the phosphorylation level of MAP2K7 also increased upon EGF stimulation (Figure S20B, Supporting Information), which accelerated the acquisition of the tumor heat-resistant phenotype to some extent. However, cetuximab did not inhibit the activation of MKK7 by EGF due to MDA-MB-231 cells are not EGFR-dependent cell line. Furthermore, we mapped the protein expression profiles of CAFs^{HR} and CAFs and found that MKK and ROCK protein expression was significantly elevated in CAFs^{HR} (Figure S20C, Supporting Information). Subsequent Gene Set Enrichment Analysis (GSEA) suggested that CAFs^{HR} had increased MAP kinase activity, ERK1 and ERK2 cascade regulation, and MAPK cascade pathway activity (Figure 7J; Figure S20D, Supporting Information). As mentioned earlier, ATF4 is an essential marker of CAF stress and regulates serine synthesis. Therefore, as expected, ATF4 expression was increased in CAFs^{HR} (Figure 7K). The GSEA results also confirmed the greater enrichment of serine metabolism in CAFs^{HR} (Figure S20E, Supporting Information). We further evaluated the clinical translational value of MAP2K7 (MKK7) based on the FUSCC (Fudan universtiy shanghai cancer center) clinical cohort system. Through multivariate Cox regression analysis, it was found that the positive expression level of MKK7 in tumor tissues (including the positive rate and the proportion of positive area) did not show a statistically significant association with the long-term prognosis of patients (Figure S21A, Supporting Information). It was worth noting that in order to eliminate the potential interference of tumor volume changes after treatment on the results, we used the pathological Miller-Payne grade as the treatment response evaluation model. The quantitative analysis results showed that a significantly increased expression intensity of MKK7 protein was observed in the group with poor treatment response (Figure S21B,C, Supporting Information). This discovery suggested that MKK7 may affected the therapeutic effect by regulating the stress response pathway of tumor cells, providing a valuable theoretical basis for exploring its application in the clinical sensitization therapy of PTT.

3. Discussion

In this study, we identified the pivotal role of cancer-associated fibroblasts (CAFs) in photothermal therapy (PTT) resistance. Within the context of precision medicine, we confirmed that ECM CAFs constitute the primary subtype involved in this resistance. Given the high expression of sigmar-1 in ECM CAFs, we designed a low-density lipoprotein (LDL) delivery platform conjugated with aminoethyl anisamide (AEAA) to specifically inhibit ECM CAFs through the targeted delivery of artesunate (ARS). Remarkably, the nanoplatform achieved superior therapeutic effects upon co-delivering photothermal agent and with a single PTT treatment. We found that the specific inhibition of ECM CAFs by ARS disrupted intracellular one-carbon metabolism, thereby interfering with serine homeostasis. Additionally, serine depletion reduced the cascade of GTPase activity in the MAPK pathway in CAFs, thereby lowering postinjury stress levels. Ultimately, the ARS nanoplatform reduced the formation of ECM CAFs and the tissue resistance barrier induced by PTT. Moreover, the generation of heat-resistant CAFs in vitro validated our findings.

PTT holds great promise as a treatment modality, as it can help to overcome tumor resistance to conventional treatments and even enhance the effectiveness of immunotherapy by inducing immunogenic cell death (ICD).[83–85] Clinical trials with indocyanine green (ICG)-mediated PTT have not achieved optimal results.[5] More importantly, in clinical practice, PTT cannot reach excessively high temperatures to ablate tumors due to clinical risks and the potential to trigger an inflammatory storm.[86] In addition to previous reported roles of CAFs in tumor immunosuppression and chemotherapy resistance,[7,87] our research also reveals the involvement of CAFs in PTT resistance. Through inhibiting CAFs with our developed artesunate loaded nanoplatform, the tumor thermotolerance was destroyed and very efficient PTT treatment was achieved.Our findings revealed that inefficient PTT increases the presence of ECM CAFs within tumors, forming a resistance barrier and leading to PTT resistance. Based on our previous research, we had confirmed that artesunate exhibited almost no direct cytotoxic effects on tumor cells within specific dosage ranges but demonstrated superior efficacy in inhibiting tumor fibrosis.[27] The artesunate nanoplatform we designed can overcome PTT resistance caused by inhibiting CAFs in the tumor microenvironment, achieving excellent anti-tumor effect of PTT. Overall, the antifibrotic potential of ARS can prevent the occurrence of PTT resistance.

This study, which explored the involvement of ECM CAFs in PTT resistance, innovatively provides new metabolic and genetic therapeutic targets for PTT sensitization—serine metabolism and MAP2K7, respectively. We systematically elucidated the role and mechanisms of action of CAFs in PTT resistance, providing deeper insights for the clinical translation of PTT. Despite proposing MAP2K7 as a novel sensitization target, our study did not systematically compare the effects of MAP2K7 and HSP70 on PTT sensitization. However, as a housekeeping protein, HSP70 is extensively involved in cellular activities;[88] thus, the use of HSP70 inhibitors may lead to increased side effects.

In the clinical translation of engineered pharmaceuticals, drug biosafety stands as a crucial evaluation parameter.[89] In current clinical practice, ICG, as a well-established biological tracer, has established a comprehensive clinical application framework.[90,91] As an endogenous substance, low-density lipoprotein follows well-defined physiological metabolic pathways: after entering cells via receptor-mediated endocytosis, it is enzymatically hydrolyzed by cholesteryl esterase into free cholesterol and fatty acids, ultimately participating in lipid metabolic cycles.[92,93] Notably, artesunate has already demonstrated excellent safety profiles in high-dose administration groups during preliminary clinical trials, validated through systematic pharmacological evaluations.[94] Although artesunate, as a first-line clinical antimalarial drug, exhibits good biosafety, its application in tumor therapy is severely limited by inherent pharmacokinetic deficiencies.[95] On one hand, it has an in vivo half-life of only 0.5 h, and its excessively rapid clearance rate results in insufficient drug exposure time.[95] On the other hand, non-specific accumulation of the free drug in liver and kidney tissues during circulation (Figure S9B, Supporting Information) may induce dose-dependent toxic side effects. Of particular concern, the drug at low doses may trigger adaptive stress responses in tumor

cells.[96] which significantly restricts its clinical application value. Building on these intrinsic properties, the innovative artesunate nanoplatform system developed in this study combines the advantages of natural carriers with safe drug. It exhibits remarkable biocompatibility superiority in cytotoxicity assays and acute toxicity testing, laying a robust foundation for accelerating its clinical translation.

In summary, ECM CAFs, which are a subtype of CAFs with high serine demand and sigmar-1 expression, can be specifically inhibited by our designed ARS nanoplatform, thereby sensitizing cells to PTT. In the future, we will conduct systematic studies using MAP2K7-specific inhibitors or serine metabolism inhibitors in combination with PTT to verify their effectiveness and pave the way for clinical trials.

4. Experimental Section

Animals: All the animal experiments were performed according to protocols approved by the Department of Laboratory Animal Science, Fudan University. The mice were fed in a circadian rhythm environment (≈25 °C, 55% humidity), and food and water were freely accessible. BALB/c-Nude mice and C57BL/6JGpt mice were purchased from GemPharmatech (Nanjing, China).

Cell Lines: The human breast cancer cell lines MDA-MB-231 and MDA-MB-468 and the mouse breast cancer cell line Eo771 were purchased from ATCC; the human breast cancer immortalized CAF line was purchased from QuiCell (Shanghai); and the fibroblast line L929 was purchased from the Cell Bank/Stem Cell Bank, Chinese Academy of Sciences. MDA-MB-231 and Eo771 cells were cultured in DMEM supplemented with 10% FBS; MDA-MB-468 cells were cultured in DMEM supplemented with 10% FBS and 15% HEPES; and fibroblasts (CAFs) were cultured in DMEM-F12 supplemented with 10% FBS, insulin (5 μg mL^{-1}), EGF, FGF-2 (5 ng mL^{-1}) and hydrocortisone (100 ng mL^{-1}). For serine depletion treatment, these cells were cultured in customized DMEM (without serine and glycine) supplemented with NCT-503 (2.5 μM) with or without 10% dialyzed FBS. All the complete media were supplemented with penicillin–streptomycin. All cells were incubated in an incubator at 37 °C with 5% CO_2.

Preparation of AI-aLDL@A: The ARS-loaded dual-targeted LDL nanoplatform (AI-aLDL@A) was synthesized via the emulsion solvent evaporation method developed by our group previously.[97] The following steps were followed. First, a mixture of phospholipids, DSPE-PEG-AEAA, DSPE-PEG-ICG, triolein, oleic acid cholesterol, cholesterol (in a molar ratio of 3:3:3:2:1:1), and ARS (20 mg) was dissolved in a solution containing acetone and ethanol. Then, the Apob peptide was dissolved in Tris-HCl buffer (pH 8.05) containing sodium oleate. The peptide was added to achieve a concentration of 3% (in terms of molar ratio) relative to the total cholesterol content. The organic and aqueous phases were mixed at a volume ratio of 1:4 under high-shear mixing conditions. The resulting mixture underwent high pressure homogenization using equipment from Avestin, Canada. The organic solvents were then removed via rotary evaporation at 50 °C to yield the AI-aLDL@A nanoparticles with dual-targeting properties.

Nanoparticle Characterization: Size, zeta potential and polydispersity index (PDI) analyses: The prepared nanoparticles were suspended in deionized water and homogenized by ultrasonication. The hydrated particle size of the nanoparticles in a glass quartz dish was measured with an analyzer (Zetasizer Nano ZS90, Malvern). Furthermore, the same solution was loaded into a zeta potential dish to determine the zeta potentials of the nanoparticles. Three measurements were taken at each time point, and these values were averaged. The morphologies of the AI-aLDL@A samples were examined via field emission transmission electron microscopy (FETEM, JEM-1400, JEOL). We lyophilized the prepared ARS nanoplatform using a vacuum freeze-dryer and stored it at −20 °C. Equal masses of the powder were dissolved in deionized water at different time points (0, 1, 2, 3, and 4 w) to assess the stability of the ARS nanoplatform during a one-month storage period. Negative staining with 2% uranyl acetate was applied to improve image quality. An AI-aLDL@A suspension (2 mg, 2 mL) was placed into an ultrafiltration tube (10 kDa) for centrifugation (3500 rpm, 10 min).

The loading content was evaluated according to our previous work.[97] In brief, the supernatant in the ultrafiltration tube was collected and demulsified with methanol, the absorbance of the supernatant was determined at 222 nm, the concentration of ARS was calculated according to the previously reported standard curve,[27] after which the loading content (entrapped drug/weight of total the nanoparticles) was finally obtained. The same amount of ars nanoplatform suspensions were respectively placed in PBS solutions containing 2% Tween 80. After centrifugation at different time points, 1 mL of the solution was taken and freeze-dried, and then dissolved in pure methanol. The 2% Tween 80 PBS was freeze-dried and then methanol was added as a blank control. The absorbance of artesunate in the freeze-dried powder methanol solution at different time points was detected. Finally, the concentration was calculated by the standard curve.

Determination of critical aggregation concentration: Prepare a Nile red DMSO solution with a concentration of 1 mg mL^{-1}. Nanoparticles of different concentrations were suspended in 900 μL of PBS solution, and then 1 μL of Nile red was added to the nano-suspension. The absorbance at 636 nm in the solutions of different concentrations was measured.

Targeting Effects of the Nanomedicine In Vivo/In Vitro—In Vitro: Cells were seeded in glass bottom dishes. After adherence, the DiD-coated nanoparticles (200 μg mL^{-1}, 200 μL) were added for 4 h of incubation with gentle shaking. Free nanoparticles were removed by rinsing with PBS, and the cells were fixed with paraformaldehyde (room temperature (RT), 15 min), stained with DAPI (C1006, Beyotime) for 15 min at RT and rinsed three times with PBS. Finally, a laser confocal microscope was used for evaluation.

In Vivo: AI-aLDL@A (5 mg mL^{-1}, 200 μL) was injected intravenously, and the ICG fluorescence distribution in the mice was observed at different time points (0.5, 2, 24, and 48 h) with an optical imaging system.

Western Blot—Cell Culture: The same number of CAFs were incubated in a 6-well plate. After 12 h, the medium was discarded, and the cells were washed with PBS three times, and new medium was added. NCT-503 (S8619, Selleck) was dissolved in DMSO. After serine depletion for various durations (12, 24, 48, or 72 h), protein was extracted from the different groups.

Mouse Tissues: Tumor tissues were cut into pieces and placed in EP tubes together with steel balls for grinding. RIPA solution (500 μL) containing PMSF was added to each tube, and the tubes were placed into a tissue grinding instrument (JXFSTPRP-CL, Shanghai Jing Xin) and ground for 30 min at 4 °C (30 Hz/30 s). The supernatant was collected after centrifugation, and the protein content in the supernatant was subsequently quantified with a BCA kit (23227, Thermo Fisher Scientific). A portion of each of the mixed samples was subjected to the BCA quantitative homogenization to standardize the concentrations between samples.

Quantitative Real-Time PCR (qPCR)—Sample Preparation: The same number of CAFs were incubated in a 6-well plate. After 12 h, the medium was discarded, the cells were washed with PBS three times, and new medium was added. NCT-503 was dissolved in DMSO. Serine depletion was then performed for various durations (12, 24, 48 h, or 72 h).

Total RNA was collected via an isolation kit (Vazyme, RC11201) and transcribed to cDNA via PrimeScript (Vazyme, R323) according to the manufacturer's protocol. qPCR was performed on a real-time qPCR instrument (Applied Biosystems, QuantStudio 7 Flex) using ChamQ Universal SYBR qPCR Master Mix (Vazyme, Q711-02). β-Actin was selected as an internal reference gene for normalization, and the data were analyzed via the comparative CT method.

The gene sequences were designed with PrimerBank (https://pga.mgh.harvard.edu/primerbank/), and detailed gene sequence information resources can be found in the Table S3 (Supporting Information).

Cell Viability Assays and ELISAs: For the in vitro cell therapy experiments, the cells were seeded into 12-well plates. After 12 h, the medium was replaced with pure DMEM (1 mL) supplemented with nanodrugs. After incubation for 4 h, the laser irradiation group was subjected to laser

irradiation (1.2 W cm^{-2}, 5 min). The cells were subsequently cultured in an incubator for an additional 44 h. The supernatant was used for ELISA after centrifugation. Finally, CCK-8 reagent (CCK-8:DMEM = 1:9, 1 mL) was added to the 12-well plate for coincubation with the cells for 1 h in an incubator, after which the supernatant was transferred to a 96-well plate (100 µL per well, 4 wells/group) for analysis with an enzyme labeling instrument (Biotek, Synergy H1).

Photothermal resistance test: Equal numbers of CAFs and $CAFs^{HR}$ were seeded in a 12-well plate. After 12 h, when the cells were completely attached to the wall, the nanomedicine (200 µg mL^{-1}) was added for 4 h of incubation with gentle shaking in an incubator before laser irradiation (1.2 W cm^{-2}, 5 min). Cell viability was measured with a CCK-8 kit (BS350B, Biosharp) at different time points (24, 48, 72, and 96 h) after the end of treatment. CAFs were stained with crystal violet solution (60506ES60, Yeasen) 96 h after laser irradiation.

The samples to be tested were added to the wells of an ELISA kit (U96-1510E, U96-1511E, YoBIbio), incubated, and then washed with washing solution. The biotin-conjugated antibody was added next. After incubation, the wells were rinsed again, and the SABC complex working solution was added for further incubation. After the SABC working solution was removed by rinsing, the prepared TMB working solution was added for incubation. Finally, the suspension solution was added, and the absorbance of each well at 450 nm was measured.

Multiple Cytokine Assays: The cell supernatant was collected after centrifugation, and the cytokine concentrations were measured with a kit (RK04339, ABclonal). The data were normalized on the basis of the cell number, and a heatmap was drawn.

Cellular Immunofluorescence—Serine Depletion Sample Preparation: Cells were seeded into confocal dishes. After incubation for 12 h, the medium was replaced with DMEM (without serine or glycine) supplemented with dialyzed FBS and NCT-503 (PHGDH inhibitor). After incubation for 48 h, the cells were washed with PBS three times and fixed with 4% paraformaldehyde for 15 min. These cells were then treated with immunosealers containing Triton X-100 at RT for 1 h, incubated with the primary antibody at 4 °C overnight, and washed with TBST three times. Next, the second antibody was added to the cells for incubation at RT for 1 h, and the cells were washed with TBST three times. Finally, the cells were incubated with DAPI dye solution for 15 min at RT.

JC-1 Staining: Dissolved the dye powder in DMSO and mixed it evenly by ultrasonic waves. DMEM diluted the dye stock solution to make the final concentration 5ug mL^{-1}. After dilution, perform ultrasonic mixing again, and then add it to the petri dish to replace the original culture medium. After incubation in the incubator for 20 min, rinse with PBS (rinse three times). Finally, fresh DMEM was added for confocal fluorescence imaging.

High-resolution confocal imaging sample preparation: The cells were seeded on special slides on one side of the attached polyvinyl microspheres. The staining procedure was the same as that for confocal microscopy sample preparation. After sample preparation, fluorescence imaging was performed. Mitochondrial statistical methods were performed according to previously published methods.[98]

Evaluation of the ARS Nanoplatform Inhibitory Efficiency on CAF: CAF cells were inoculated in 6-well plates. The experiment began when the cell fusion degree reached 80%. The experimental groups were divided into the control group, the free ARS group (the total amount of drug was consistent with the drug content on the nanoplatform), the free ICG group (the total amount of ICG was calculated based on the molar mass ratio of ICG in the nanoplatform system), and the nanoplatform group (the final concentration of the medium and nanoplatform suspension was 200 µg mL^{-1}, and the culture system was 2 mL). After the drug is added, place the 6-well plate on the shaker in the cell culture incubator and gently shake it. After incubation for 4 h, discard the culture medium, rinse with PBS, and then add fresh culture medium (without FBS). The nanoplatform group and the free ICG group were irradiated with near-infrared laser (808 nm, 1.2 W cm^{-2}, 5 min). After the irradiation was completed, the cells were placed in the incubator for continued incubation for 24 h. Another way, cells in different experimental groups were incubated with the respective drugs for 48 h (the cycle in which the drug's accumulation in the tumor starts to decrease, based on in vivo targeting experimental results), while laser irradiation was still performed 4 h post-treatment, and incubated for 44 h. CCK8 assay and immunoblotting were performed.

Cell Migration Assay: CAFs were seeded in 6-well plates, and when the cells reached full confluency, a scratch was made with a pipette tip, and the complete medium was replaced with medium without FBS.

Flow Cytometry: CAFs were seeded in 6-well plates and divided into control and Depletion groups. The Depletion group was subjected to serine/glycine depletion with NCT-503 and DMEM without serine/glycine for 48 h. The cells were then treated with trypsin with EDTA. The number of cells in the two groups was consistent, as determined by cell counting. After rinsing three times with cell staining buffer (420201, BioLegend), an antibody (648003, BioLegend) was added, and the mixture was incubated at 4 °C for 30 min before rinsing again with staining buffer. Finally, the cells were examined with a flow cytometer (CytoFLEX S, Beckman Coulter).

Immunoprecipitation (IP): CAFs were seeded in 6-well plates and divided into control and Depletion groups. The Depletion group was subjected to serine/glycine depletion with NCT-503 and DMEM without serine/glycine for 48 h. Furthermore, the cells were rinsed with PBS. RIPA lysis buffer containing 1% PMSF was added, and the cells collected by scraping. The supernatant was collected after centrifugation (12 000 rpm, 15 min, 4 °C). Magnetic beads (HY-K0202) were rinsed with PBS and then incubated with an anti-HSP70 antibody (ab182844, Abcam). After coupling, rinsing was performed again to remove free antibodies. Furthermore, the antibody-conjugated magnetic beads were mixed with the extracted protein mixture overnight at 4 °C, after which the magnetic beads were separated from the protein mixture with a magnetic rack and the supernatant was removed. The magnetic beads were rinsed 6 times. The proteins from the magnetic beads were separated with elution buffer (room temperature, 5 min), and neutralization buffer was used to terminate the reaction. The isolated protein mixture was evaluated via mass spectrometry.

Validation of the Involvement of MAP2K7 in PTT Resistance: Equal numbers of CAFs were seeded in 6-well plates or 96-well plates, and the medium was changed to serum-free medium after 24 h. DTP3 (HY-100538, MCE) was added to the culture medium (15 µM) as an MKK7 inhibitor. After 12 h of incubation, free ICG (final concentration 100 µg mL^{-1}) was added, and the cells were incubated again for 4 h before laser irradiation. Twelve hours later, the cells were washed with PBS to remove free cells, and the remaining cells were incubated with crystal violet stain or CCK-8 solution.

Equal numbers of CAFs were seeded in 6-well plates and grouped according to the different treatments. The groups included the control group, the EGF group (medium supplemented with 25 ng mL^{-1} EGF (RP01030, ABclonal)), and the TKI group (medium supplemented with 50 µg mL^{-1} cetuximab (A2000, Selleck)); each culture system was 2 mL. Drug treatment for protein immunoblot assessment was performed after 24 h.

Sample Purification: The sample number varied on the basis of the sequencing method due to the fragmentation of a single tumor into multiple tissue fragments. Therefore, sequencing every tissue fragment might have resulted in multiple sequencing of certain tumor samples.

Total RNA from Cell/Tissue Samples: Total RNA was extracted according to the instructions of the miRNA isolation kit (AM1561, Thermo Fisher) and purified by magnetic bead separation (A63881, Beckman Coulter). Then, cDNA was synthesized with a SuperScript II Reverse Transcriptase Kit (18064014, Invitrogen). Finally, the samples were evaluated with a bioanalyzer (Agilent 2100, Agilent).

Total Protein from Cell/Tissue Samples: The protein extraction method was the same as that used for Western blotting. DTT was added to the protein mixture, which was subsequently incubated for 30 min at 55 °C. An equal volume of iodoacetamide was then added for 15 min of incubation at RT. Subsequently, six volumes of acetone were added, and each mixture was incubated at −20 °C for 4 h. The precipitate was collected by centrifugation and redissolved in tetraethylammonium bromide (TEAB). The protein was digested with trypsin-TPCK (1/50 by protein weight) overnight.

Total Metabolites in the Cell/Tissue Samples: The tissues were cut into pieces, mixed with a 4:1 (vol/vol) methanol:water solution in tubes and ground with grinding balls to extract the metabolites. The weight of each tissue sample was the same.

SILAC: CAFs were seeded in culture dishes and allowed to adhere. The medium was replaced with serine depletion medium (DMEM without serine/glycine supplemented with NCT-503 and 10% FBS), and then ^{13}C-labeled L-serine (IR-30150, IsoReag) (42 mg L^{-1}) was added. The cells were incubated for 12 h or 48 h, and protein extraction was performed as described for protein mass spectrometry. Finally, the proteins were subjected to mass spectrometry analysis (Orbitrap Exploris 480, Thermo Fisher Scientific).

Transfection of Small Interfering RNA In Vivo and In Vitro—In Vitro: Cells were inoculated in 6-well plates. After adhesion, when the cell fusion degree reached 60%, a mixture of siRNA was added. The small interfering RNA was customized by GenePharma (Shanghai) and used at a concentration of 20 µM after being added to ddH_2O. Take 5 µL RNA stock solution and add it to 150 µL of opti-MEM; After mixed well, then add 5 µL of transfection reagent and mix well again. Incubate at room temperature for 15 min. Finally, add it to a 6-well plate, mix well and incubate for 48 h before extracting the protein.

In Vivo: After establishing tumor xenografts through co-implantation of CAFs and MDA-MB-231 cells, mice were randomly divided into two groups: Control group and siRNA group. The siRNA group received peritumoral subcutaneous injections of 100 µL mixture containing chemically modified siRNA (Gene Pharma, Shanghai) complexed with in vivo transfection reagent (Gene Pharma, Shanghai) at a 2:1 ratio (µg:µL), while the Control group received subcutaneous injections of transfection reagent alone (without siRNA). After 48 h, both groups were administered equivalent volumes of AI-aLDL@A suspension via tail vein injection. In vivo imaging was performed 24 h post-injection.

Liquid Chromatography–Tandem Mass Spectrometry (LC–MS/MS) Analysis: The peptides were suspended in 0.1% formic acid (FA) for analysis via a TIMS-TOF Pro mass spectrometer (timsTOF Pro, Bruker). The chromatographic conditions were as follows: an optics column (25 cm long, 75 µm ID packed with 1.6 µm C18) was used, the column temperature chamber was set to 50 °C, the elution flow rate was 300 nL min^{-1}, and the total elution time was 60 min. Chromatographic separation was performed with Solvent A (0.1% FA in water) and Solvent B (80% acetonitrile with 0.1% FA) with gradient elution of the peptides as follows: 2–22% B from 045 min, 22–37% B from 45 to 50 min, 37–80% B from 50 to 55 min, and maintained at 80% B for the last 5 min. The mass spectrometry parameters were as follows: scan range, 100–1700 m z^{-1}; 1/k0 range, 0.7–1.3; PASEF, 10; intensity threshold, 5000; accumulation and ramp time, 100 ms; capillary voltage, 1500 V; DRY gas, 3 L min^{-1}; and temperature, 180 °C.

The Thermo Q Exactive HF system (Xcalibur, Thermo Scientific) was operated in full MS scan mode for data acquisition (acquisition from m/z 50750) and an initial MS spectrum was acquired to quantify each biological sample for metabolite. Then, data-dependent acquisition (DDA) was performed with the following parameters: MS scan time, 50 ms per scan; and resolution: 60000; and MS/MS scan time, 50 ms per scan; and resolution, 15000. The top 10 most intense ions were selected for fragmentation (30 NCE). The ESI source parameters were set as follows: spray voltage, 3.5 kV; capillary temperature, 320 °C; aux gas heater temperature, 300 °C; sheath gas flow, 45 L h^{-1}; and aux gas flow, 10 L h^{-1} (Table S6, Supporting Information).

The data were analyzed by PEAKS Online (Bioinformatics Solutions Inc., version 1.5).

LC–MS/MS Data Processing: The raw data files acquired by the timsTOF Pro instrument were analyzed by PEAKS online software (https://www.bioinfor.com/, Bioinformatics Solutions Inc., PEAKS Online X build). Human-derived protein data (*Homo sapiens*, downloaded in July 2022, containing 20381 reviewed human-derived proteins) from the UniProt Swiss-Prot database (https://www.uniprot.org/) were used.

Animal Experiments: High-fibrosis mouse breast cancer model: CAFs were mixed with MDA-MB-231 cells (10^6) in PBS at a ratio of 1:4, after which the suspensions were mixed with Matrigel (1:1, vol/vol). The final solution was injected into the mouse breast pad.

In Vivo Therapeutic Experiments: Mice (n = 48) were randomly divided into 8 groups (control, LDL, I-LDL+L, LDL@A+L, I-LDL@A+L, A-aLDL@A, AI-aLDL+L, and AI-aLDL@A+L). The tumor cell and Matrigel suspension (1:1, vol/vol) was injected into the breast pads of the mice. AI-aLDL@A was administered at a dosage of 10 mg mL^{-1}, 200 µL/3 days, and the dosages of the other drugs were determined according to the previously calculated drug loading. PTT was not performed after the first drug administration. Two hours after the second administration, the tumor was irradiated with an 808 nm laser (1.2 W cm^{-2}) for 5 min. The temperature changes in the tumors were monitored during PTT. The tumor volume (long diameter: a; minor axis: b) and body weight of the mice were measured before each administration. Tumor volume was calculated via the following formula: $volume = 1/2ab^2$. The lengths and widths of unrecognized tumors were defined as 0.5 mm.

In Vivo Evaluation of the Involvement of CAFs in PTT Resistance: CAFs and MDA-MB-231 cells (10^6 MDA-MB-231 cells with a CAF:MDA-MB-231 cell ratio of 1:4) were mixed in a mixture of PBS and matrix gel (1:1, vol/vol), and the resulting cell suspension was seeded in the breast pads of nude mice. When the tumor size reached 300 mm^3, the mice were subjected to laser irradiation (1 W cm^{-2}, 2 min) 2 h after injection of free ICG (1 mg mL^{-1}, 100 µL). Six days later, all the mouse tumors were collected, weighed and measured. All procedures were completed within 12 days after tumor inoculation.

In Vivo Assessment of Tumor Fibrosis Induced by PTT: Mice (C57BL/6J, n = 4; 4-weeks old) were randomly divided into two groups (control and PTT), and a cell suspension (10^6 total cells, PBS:Matrigel = 1:1 (vol/vol), 100 µL) was injected into the right third pair of mammary pads. When the tumors grew to 200 mm^3, the mice in the PTT group were injected with PBS, and the mice in the PTT group were injected with free ICG (1 mg mL^{-1}, 100 µL) via the tail vein. Two hours after injection, the tumor site was irradiated with a laser (808 nm, 1 W, 2 min). Seventy-two hours later, the mouse tumor tissues were harvested for protein extraction and MS analysis.

ARS Nanoplatform In Vivo Toxicity Assessment: The mice were randomly divided into three groups: the control group did not receive any treatment; the ARS nanoplatform group received the nanosuspension (10 mg mL^{-1}, 200 µL); and the free ARS group received free ARS solution via the tail vein (the same amount of ARS was administered as that in the nanoplatform group after conversion according to the loading content). Blood samples were taken 72 h later to assess indicators of liver and kidney function.

Serine depletion sensitize the efficacy of PTT in vivo: Eo771 tumor-bearing C57/BL6J mouse models were established and subsequently randomized into two treatment groups: PTT group and combination therapy group. PTT group: Intravenous administration of free ICG via tail vein injection, followed by NIR laser irradiation at the tumor site 2 h post-injection. combination therapy group: Pretreatment with NCT-503 (50 mg kg^{-1}, intraperitoneal injection, once/2 days, vehicle: 2% DMSO, 40% PEG300, 5% Tween-80, 53% water) prior to PTT. Subsequent ICG administration and laser irradiation parameters matched those of the PTT group. Six days later, all the mouse tumors were collected, weighed and measured (The scab at the tumor site was removed and weighed).

Preparation of Serum: A capillary tube containing heparin was inserted into the inner canthus of the mouse eye, and the drained blood was collected in an EP tube containing EDTA-K2. The blood was allowed to stand at room temperature for 1 h, and then the serum was collected after centrifugation. Serum cytokines were detected with a kit (RK04382, ABclonal).

Quantitative Immunohistochemical Analysis: The immunohistochemical image was transformed into an RGB-stack image, and the contrast was adjusted. Furthermore, the threshold was set to ensure that the positive area was consistent with the setting range. Finally, quantitative analysis was performed.

Evaluation of the Penetration Efficiency of ars Nanoplatform in Highly Fibrotic Tumors: We established a co-culture model of CAFs and MDA-MB-231 in nude mice. Post-tumor formation, mice received tail vein injections of Cy5-loaded nanoplatform formulations (5 mg mL^{-1}, 100 µL). Four hours post-injection, tumor tissues were harvested, surface fluids removed using absorbent paper, embedded in OCT compound, and sectioned for fluorescence imaging. To preserve nanoplatform structural integrity, fresh-frozen tissue sections were directly imaged without further processing.

Tissue Sectioning and Immunohistochemistry: Tissue sections for immunohistochemical staining were prepared by professional technicians. The technicians were blinded the tissue grouping information during the process, providing only technical assistance and not participating in the analysis.

Clinical Sample Cohort: The tissue samples were collected from the tissue bank of Fudan University Shanghai Cancer Center (FUSCC). All samples were pathologically diagnosed as triple-negative breast cancer. The use of clinical information and tissue use has been approved by the Ethics Committee of Shanghai Cancer Center, Fudan University, with the ethics number FUSCC-IACUC-S2025-0516. All patients had received chemotherapy or/and immunotherapy before the tumor specimens were obtained through surgery.The classification of treatment response is differentiated according to the pathological Miller-Payne classification system. Whole-slide imaging analysis was performed using Visiopharm AI-powered platform, with rigorous normalization of staining intensity across batches.

Sample Preparation for Spatial Omics: After the tumor tissue of each mouse was removed, the excess body fluid in the tumor tissue was removed by blotting with absorbent paper. The samples were subsequently embedded in optimal cutting temperature (OCT) compound and stored at −80 °C before cryosectioning.

Bioinformatics Analysis—Single-Cell RNA Sequencing (scRNA-seq) Data Sources and Grouping: scRNA-seq data were derived from studies previously published by our group.[27] The tumor tissue types determined from Eo771 tumor-bearing C57BL/6J mice. The control group did not receive any treatment, while the PD-1 group was treated with a PD-1 monoclonal antibody (10 mg kg^{-1}, twice a week) before the tumor tissues were obtained. The mice in the combined treatment group were injected with ARS-loaded poly(lactic-co-glycolic acid) (PLGA) coated with TNBC cell membrane biomimetic nanoparticles (20 mg mL^{-1}, 200 µL, once every 3 days) combined with the PD-1 monoclonal drug (10 mg kg^{-1}, twice a week) via the tail vein. Tumor tissues were harvested after 18 days of monitoring for scRNA-seq. Two independent biological samples were collected from each group.

Spatial transcriptomics sequencing was performed via the 10x Genomics Visium Spatial Transcriptomics platform, which captures mRNAs on the basis of polyA sequences. Frozen sections (10 µm thick) containing the target region were mounted on 10x Visium Spatial slides, followed by methanol fixation, H&E staining, and image scanning according to the protocol recommended by 10x Genomics. Subsequently, tissue permeabilization, reverse transcription, cDNA amplification, and DNA library construction were carried out via the 10x Genomics Visium Spatial Gene Expression Slide & Reagent Kit (PN-1000184) and Visium Spatial Gene Expression Slide Kit (PN-1000185) following the manufacturer's instructions. Qualified DNA libraries were subjected to high-throughput sequencing via PE150 mode.

Spatial Metabolic Sequencing: The experiment was conducted via the AFADESI-MSI platform (Beijing Victor Technology Co., Ltd., Beijing, China) in tandem with a Q-Orbitrap mass spectrometer (Q Exactive, Thermo Scientific, U.S.A.). In negative ion mode, the spray solvent was acetonitrile (ACN)/H_2O (8:2), and in positive ion mode, the spray solvent was ACN/H_2O (8:2, 0.1% FA). The solvent flow rate was 5 µL min^{-1}, the transport gas flow rate was 45 L min^{-1}, the spray voltage was set at 7 kV, and the distance between the sample surface and the sprayer, as well as between the sprayer and the ion transport tube, was 3 mm. The MS resolution was set at 70000, with a mass range of 70–1000 Da, an automated gain control (AGC) target of 2E6, a maximum injection time of 200 ms, an S-lens voltage of 55 V, and a capillary temperature of 350 °C. During MSI analysis, the speed in the X direction was 0.2 mm s^{-1} with a vertical step size of 100 µm in the Y direction. Using imzMLConverter,[99] the raw MS data files in.raw format were converted to.imML format to be imported into MSiReader, an open source software for viewing and analyzing high-resolution MS image files on the MATLAB platform. After background subtraction via the Cardinal package,[100] ion image reconstruction was performed. All mass spectrometry images were normalized using total ion count (TIC) per pixel.[101] High-spatial-resolution H&E images were matched to precisely extract region-specific MS profiles. Differentially abundant metabolites in different tissue microregions were first screened via the supervised statistical method orthogonal partial least squares discriminant analysis (OPLS-DA). The variable importance of projection (VIP) values obtained from the OPLS-DA model were used to describe the overall contribution of each metabolite to group differentiation. A VIP value greater than 1 indicated that the metabolite could be a potential differentially abundant metabolite. Furthermore, a two-tailed Student's t test was used to determine whether the differentially abundant metabolite was significant. Finally, metabolites with VIP values greater than 1.0 and *P* values less than 0.05 were selected as differentially abundant metabolites. Additionally, owing to the special data structure obtained from MSI analysis, we performed dimensionality reduction on the MS data for each pixel via T-distributed stochastic neighbor embedding (t-SNE) and uniform manifold approximation and projection (UMAP). For MSI data clustering, we adopted the spatial shrunken centroid clustering (SSCC) algorithm to cluster the samples on the basis of the differences in ion abundance in each pixel.

GSEA: Gene sets in corresponding pathways were obtained from Gene Ontology (GO) and Kyoto Encyclopedia of Genes and Genomes (KEGG), and enrichment scores were determined according to the expression of corresponding genes in the two groups of samples. The gene set number range was 5–500.

RTCD Analysis: RCTD[102] (version 1.1.0) is a robust cell type decomposition method that uses cell type profiles obtained from single-cell RNA-seq data to decompose mixtures of cell types while correcting for differences across sequencing technologies. The create.RCTD function was used with the default parameters to ensure that each cell type has at least one cell and that each spot has at least one unique molecular identifier (UMI). The run.RCTD function is set with doublet_mode as FALSE to infer the composition of the cell types in each spot.

Metascape: The proteins whose expression was lower in the A-aLDL@A group than in the control group were entered into Metascape (https://metascape.org/gp/index.html#/main/step1) for enrichment analysis.[103]

Signature Score Analysis: The function calculates the average expression level of all genes in the gene set at the single-cell level, and then cuts the expression matrix into several parts according to the average value, and randomly selects the background value of the control gene from each copy after subtracting.

Macrophage Polarization Score: The expression levels of macrophage cell populations in different genes were scored for polarization. M1 polarization markers: *Tnf*, *Il6*, *Cd86*, *Il1b*, *Nos2*, *Cd80*, *Cxcl10*, *Cd86*, *Il1a*,*Ccl5*, *Irf1*, *Cd40*, *Ido1*, *Kynu*, *Ccr7*; M2 polarization markers: *Arg1*, *Arg2*, *Il10*, *Cd163*, *Cd200r1*, *Pdcd11g2*, *Cd274*, *Csflr*, *Il1r2*, *Il4ra*, *Ccl4*, *Ccl2*, *Ccl20*, *Ccl22*, *Ccl24*, *Lyve1*, *Vegfa*, *Vegfb*, *Vegfc*, *Egf*, *Ctsa*, *Ctsb*, *Ctsd*, *Tgfb1*, *Tgfb2*, *Tgfb3*, *Mmp14*, *Mmp19*, *Mmp9*,*Clec7a*, *Wnt7b*, *Tnfsf8*, *Cd276*, *Vtcn1*, *Msr1*, *Fn1*, *Irf4*.

Cell Chat Analysis: CellChat (version 1.1.3) R package was used for cell-to-cell ligand-receptor interaction analysis. First, the normalized expression matrix was imported and the cellchat object was created through the createCellChat function. Use the default parameters through identifyOverExpressedGenes, identifyOverExpressedInteractions and preprocessing operations projectData function; The computeCommunProb, filterCommunication (min.cells = 10) and computeCommunProbPathway functions were used to calculate potential ligand-receptor interactions. Finally, the intercellular communication network is aggregated by aggregateNet function.

scMetabolism Analysis: scMetabolism (version 0.2.1) is based on the conventional single-cell transcriptome expression matrix file, and uses the VISION algorithm to score each cell, and finally obtains the activity score of cells in each metabolic pathway. The software presets the human metabolic gene set, including 85 KEGG pathways and 82 REACTOME entries. If the species was mammals such as rats and mice, the analysis was carried out after homologous transformation.

Materials: All information related to the antibodies, reagents, and instruments used in this study are given in Tables S1–S5 (Supporting Information).

Statistical Analysis: Data were collected from at least two independent experiments and are expressed as the mean ± S.E.M. values. Differences between groups were determined with *t* tests.

Supporting Information

Supporting Information is available from the Wiley Online Library or from the author.

Acknowledgements

The authors are grateful to Xiaochun Wan M.D. (Fudan University Shanghai Cancer center) for her evaluation recommendations on all tissue sections, Qian Zhou Ph.D., Siyi Cao Ph.D. and Fan Yang Ph.D. (Fudan University Shanghai Cancer center), Zhiguo Zhou Professor (Shanghai Normal University) for critically reading the manuscript. The authors also thank to Lian Li, Xiaohua Yao (Shanghai OEbiotech Co., Ltd. (Shanghai, China)) and Zhenyu Xu (Shanghai Lu Ming Biotech Co., Ltd. (Shanghai, China)) for their assistance in spatial omics and sc-RNA seq analysis. This study was supported by the National Science Foundation (Grant No. 82372145 (H.Z.)), the Joint Fund of the Zhejiang Provincial Natural Science Foundation of China (Grant No. BD24H180004 (H.Z.)), and the grant from the Discipline Cluster of Oncology, Wenzhou Medical University, China (Grant No. z1-2023002 (H.Z.)). It was also supported by the Research Project (Grant No. 347897 (H.Z.)), Solution for Health Profile (Grant No. 336355 (H.Z.)), InFLAMES Flagship (Grant No. 337531 (H.Z.)) and Printed Intelligence Infrastructure (PII-FIRI) from Research Council of Finland. The National Natural Science Foundation of China (Grant No. 82071945, 82371978, 82311530049 (S.Z.)), Shanghai Committee of Science and Technology, China (Grant No. 21S31905400 (S.Z.)), the National Natural Science Foundation of China (Grant No. 81830058 (C.C.)), and the Shanghai Anticancer Association EYAS PROJECT (Grant No. SACA-CY22C07 (D.Z.)), China Postdoctoral Science Foundation (Grant No. 2024M760561 (D.Z.))

Open access publishing facilitated by Abo Akademi, as part of the Wiley - FinELib agreement.

Conflict of Interest

The invention of the heat-resistant CAF-inducing method, the use of MAP2K7 as a photothermal sensitizing target, and the use of ARS in TNBC sensitizing therapy were the subject of Chinese patent applications 2023108836307, 2023112194149, and 202311069334X by D.Z., S.Z., and C.C. The remaining authors declare no conflict of interest.

Author Contributions

D.Z., J.Y., X.L., and Z.Z. contributed equally to this work. D.Z. and H.Z. performed conceptualization; D.Z., J.Y., X.L., Y. Z., H.H., Z.W., C.C., S.Z., and H.Z. performed methodology; D.Z., J.Y., X.L., Z.Z., M.Q., L.B., J.Z., A.J., Z.W., B.F., and X.Q. performed investigation; D.Z., J.Y., X.L., Z.Z., Y.Z., H.H., and W.S. performed visualization; D.Z., X.L., B.F., and Y.Z. performed protein spectrum test & analysis; D.Z., Z.Z., A.J., Z.W., S.W., and W.S. performed animal experiment: D.Z., X.L., B.F., Y.Z., and C.D. performed bioinformatic analysis; J.Y., D.Z., and H.Z. performed nanomedicine design; D.Z., C.C., S.Z., and H.Z. performed funding acquisition; C.C., S.Z., and H.Z. performed supervision; D.Z., J.Y., X.L., and Z.Z. wrote original draft; D.Z., J.Y., X.L., Z.Z., C.C., S.Z., and H.Z. wrote, reviewed, and edited.

Data Availability Statement

The data that support the findings of this study are available in the supplementary material of this article.

Keywords

artesunate nanoplatform, breast cancer, cancer-associated fibroblasts, photothermal therapy

Received: February 8, 2025
Revised: May 31, 2025
Published online:

[1] J. Li, H. Tian, F. Zhu, S. Jiang, M. He, Y. Li, Q. Luo, W. Sun, X. Liu, P. Wang, *Adv. Healthcare Mater.* **2022**, *11*, 2201986.
[2] L. Xu, W. Zhang, H. B. Park, M. Kwak, J. Oh, P. C. W. Lee, J. O. Jin, *J. ImmunoTher. Cancer* **2019**, *7*, 220.
[3] J. S. Ni, X. Zhang, G. Yang, T. Kang, X. Lin, M. Zha, Y. Li, L. Wang, K. Li, *Angew. Chem., Int. Ed.* **2020**, *59*, 11298.
[4] X. Li, J. F. Lovell, J. Yoon, X. Chen, *Nat. Rev. Clin. Oncol.* **2020**, *17*, 657.
[5] X. Li, G. L. Ferrel, M. C. Guerra, T. Hode, J. A. Lunn, O. Adalsteinsson, R. E. Nordquist, H. Liu, W. R. Chen, *Photochem. Photobiol. Sci.* **2011**, *10*, 817.
[6] O. Elhanani, R. Ben-Uri, L. Keren, *Cancer Cell* **2023**, *41*, 404.
[7] Y. Chhabra, A. T. Weeraratna, *Cell* **2023**, *186*, 1580.
[8] J. M. Pitt, A. Marabelle, A. Eggermont, J. C. Soria, G. Kroemer, L. Zitvogel, *Ann. Oncol.* **2016**, *27*, 1482.
[9] D. Öhlund, E. Elyada, D. Tuveson, *J. Exp. Med.* **2014**, *211*, 1503.
[10] H. F. Dvorak, *Semin. Thromb. Hemost.* **2019**, *45*, 576.
[11] R. Straussman, T. Morikawa, K. Shee, M. Barzily-Rokni, Z. R. Qian, J. Du, A. Davis, M. M. Mongare, J. Gould, D. T. Frederick, Z. A. Cooper, P. B. Chapman, D. B. Solit, A. Ribas, R. S. Lo, K. T. Flaherty, S. Ogino, J. A. Wargo, T. R. Golub, *Nature* **2012**, *487*, 500.
[12] D. Fukumura, R. Xavier, T. Sugiura, Y. Chen, E.-C. Park, N. Lu, M. Selig, G. Nielsen, T. Taksir, R. K. Jain, B. Seed, *Cell* **1998**, *94*, 715.
[13] G. Tortora, R. Bianco, G. Daniele, F. Ciardiello, J. A. McCubrey, M. R. Ricciardi, L. Ciuffreda, F. Cognetti, A. Tafuri, M. Milella, *Drug Resist. Updates* **2007**, *10*, 81.
[14] E. J. Morris, S. Jha, C. R. Restaino, P. Dayananth, H. Zhu, A. Cooper, D. Carr, Y. Deng, W. Jin, S. Black, B. Long, J. Liu, E. DiNunzio, W. Windsor, R. Zhang, S. Zhao, M. H. Angagaw, E. M. Pinheiro, J. Desai, L. Xiao, G. Shipps, A. Hruza, J. Wang, J. Kelly, S. Paliwal, X. Gao, B. S. Babu, L. Zhu, P. Daublain, L. Zhang, et al., *Cancer Discov.* **2013**, *3*, 742.
[15] L. Wang, L. Oliveira, H. R., B. S., P. E., B. N., B. D., S. A., Z. J.-Y., L.-V. J., et al., *Cell* **2018**, *173*, 1413.
[16] C. Alter, A.-S. Henseler, C. Owenier, J. Hesse, Z. Ding, T. Lautwein, J. Bahr, S. Hayat, R. Kramann, E. Kostenis, J. Scheller, J. Schrader, *J. Clin. Investig.* **2023**, *133*, 163799.
[17] D.-M. Xiang, W. Sun, B.-F. Ning, T.-F. Zhou, X.-F. Li, W. Zhong, Z. Cheng, M.-Y. Xia, X. Wang, X. Deng, W. Wang, H.-Y. u. Li, X.-L. Cui, S.-C. Li, B. Wu, W.-F. Xie, H.-Y. Wang, J. Ding, *Gut* **2018**, *67*, 1704.
[18] X. Hou, S. Yin, R. Ren, S. Liu, L. Yong, Y. Liu, Y. Li, M. H. Zheng, G. Kunos, B. Gao, H. Wang, *Hepatology* **2021**, *74*, 116.
[19] M. Verheij, R. Bose, X. Hua Lin, B. Yao, W. D. Jarvis, S. Grant, M. J. Birrer, E. Szabo, L. I. Zon, J. M. Kyriakis, A. Haimovitz-Friedman, Z. Fuks, R. N. Kolesnick, *Nature* **1996**, *380*, 75.
[20] T. Moriguchi, F. Toyoshima, N. Masuyama, H. Hanafusa, Y. Gotoh, E. Nishida, *EMBO J.* **1997**, *16*, 7045.
[21] T. Tan, H. Hu, H. Wang, J. Li, Z. Wang, J. Wang, S. Wang, Z. Zhang, Y. Li, *Nat. Commun.* **2019**, *10*, 3322.
[22] D. Zheng, Y. H. W. C., L. Xu, Q. Dong, C. Du, J. Du, F. Li, *Int. J. Nanomed.* **2020**, *15*, 10007.
[23] X. Liu, Y. Lu, J. Huang, Y. Xing, H. Dai, L. Zhu, S. Li, J. Feng, B. Zhou, J. Li, Q. Xia, J. Li, M. Huang, Y. Gu, S. Su, *Cancer Cell* **2022**, *40*, 1341.

[24] Y.-Z. Jiang, D. Ma, C. Suo, J. Shi, M. Xue, X. Hu, Y. i. Xiao, K.-D. Yu, Y.-R. Liu, Y. Yu, Y. Zheng, X. Li, C. Zhang, P. Hu, J. Zhang, Q. Hua, J. Zhang, W. Hou, L. Ren, D. Bao, B. Li, J. Yang, L. Yao, W.-J. Zuo, S. Zhao, Y. Gong, Y.-X. Ren, Y.-X. Zhao, Y.-S. Yang, Z. Niu, et al., *Cancer Cell* **2019**, *35*, 428.
[25] Y. Xiao, D. Ma, Y.-S. Yang, F. Yang, J.-H. Ding, Y. Gong, L. Jiang, L.-P. Ge, S.-Y. Wu, Q. Yu, Q. Zhang, F. Bertucci, Q. Sun, X. Hu, D.-Q. Li, Z.-M. Shao, Y.-Z. Jiang, *Cell Res.* **2022**, *32*, 477.
[26] Y. Chen, K. M. McAndrews, R. Kalluri, *Nat. Rev. Clin. Oncol.* **2021**, *18*, 792.
[27] D. Zheng, J. Zhou, L. Qian, X. Liu, C. Chang, S. Tang, H. Zhang, S. Zhou, *Bioact. Mater.* **2023**, *22*, 567.
[28] Z. Wang, S. Li, M. Zhang, Y. Ma, Y. Liu, W. Gao, J. Zhang, Y. Gu, *Adv. Sci.* **2016**, *4*, 1600327.
[29] S. Song, Q. i. Wang, J. Xie, J. Dai, D. Ouyang, G. Huang, Y. Guo, C. Chen, M. Wu, T. Huang, J. Ruan, X. Cheng, X. Lin, Y. u. He, E. A. Rozhkova, Z. Chen, H. Yang, *Adv. Healthcare Mater.* **2023**, *12*, 2301437.
[30] Z. Chen, S. Li, F. Li, C. Qin, X. Li, G. Qing, J. Wang, B. Xia, F. Zhang, L. Meng, X.-J. Liang, Y. Xiao, *Adv. Sci.* **2023**, *10*, 2206707.
[31] G. Biffi, D. A. Tuveson, *Physiol. Rev.* **2020**, *101*, 147.
[32] F. Valdés-Mora, R. Salomon, B. S. Gloss, A. M. K. Law, J. Venhuizen, L. Castillo, K. J. Murphy, A. Magenau, M. Papanicolaou, L. Rodriguez de la Fuente, D. L. Roden, Y. Colino-Sanguino, Z. Kikhtyak, N. Farbehi, J. R. W. Conway, N. Sikta, S. R. Oakes, T. R. Cox, S. I. O'Donoghue, P. Timpson, C. J. Ormandy, D. Gallego-Ortega, *Cell Rep.* **2021**, *35*, 108945.
[33] I. I. Verginadis, H. Avgousti, J. Monslow, G. Skoufos, F. Chinga, K. Kim, N. M. Leli, I. V. Karagounis, B. I. Bell, A. Velalopoulou, C. S. Salinas, V. S. Wu, Y. Li, J. Ye, D. A. Scott, A. L. Osterman, A. Sengupta, A. Weljie, M. Huang, D. Zhang, Y. Fan, E. Radaelli, J. W. Tobias, F. Rambow, P. Karras, J.-C. Marine, X. Xu, A. G. Hatzigeorgiou, et al., *Nat. Cell Biol.* **2022**, *24*, 940.
[34] R. Rapetti-Mauss, J. Nigri, C. Berenguier, P. Finetti, S. S. Tubiana, B. Labrum, B. Allegrini, B. Pellissier, G. Efthymiou, Z. Hussain, C. Bousquet, N. Dusetti, F. Bertucci, H. Guizouarn, P. Melnyk, F. Borgese, R. Tomasini, O. Soriani, *Gut* **2023**, *72*, 722.
[35] Y. Yao, Q. Guo, Y. Cao, Y. Qiu, R. Tan, Z. Yu, Y. Zhou, N. A. LuO, *J. Exp. Clin. Cancer Res.* **2018**, *37*, 282.
[36] D. Crottès, R. Rapetti-Mauss, F. Alcaraz-Perez, M. Tichet, G. Gariano, S. Martial, H. Guizouarn, B. Pellissier, A. Loubat, A. Popa, A. Paquet, M. Presta, S. Tartare-Deckert, M. L. Cayuela, P. Martin, F. Borgese, O. Soriani, *Cancer Res.* **2016**, *76*, 607.
[37] M. Hu, Y. Wang, Z. Liu, Z. Yu, K. Guan, M. Liu, M. Wang, J. Tan, L. Huang, *Nat. Nanotechnol.* **2021**, *16*, 466.
[38] S. S. Talsma, J. E. Babensee, N. Murthy, I. R. Williams, *J. Controlled Release* **2006**, *112*, 271.
[39] P. Zhou, S. Hatziieremia, M. A. Elliott, L. Scobie, C. Crossan, A. M. Michie, T. L. Holyoake, G. W. Halbert, H. G. Jørgensen, *J. Controlled Release* **2010**, *148*, 380.
[40] S. Hayavi, G. W. Halbert, *Biotechnol. Prog.* **2005**, *21*, 1262.
[41] J. Y. Lee, J. H. Kim, K. H. Bae, M. H. Oh, Y. Kim, J. S. Kim, T. G. Park, K. Park, J. H. Lee, Y. S. Nam, *Small* **2015**, *11*, 222.
[42] W. Li, J. Fu, Y. Ding, D. Liu, N. Jia, D. Chen, H. Hu, *Acta Biomater.* **2019**, *96*, 456.
[43] D. Sobot, S. Mura, M. Rouquette, B. Vukosavljevic, F. Cayre, E. Buchy, G. Pieters, S. Garcia-Argote, M. Windbergs, D. Desmaële, P. Couvreur, *Mol. Ther.* **2017**, *25*, 1596.
[44] W. She, K. Luo, C. Zhang, G. Wang, Y. Geng, L. Li, B. He, Z. Gu, *Biomaterials* **2013**, *34*, 1613.
[45] W. Z. Dang, H. Li, B. Jiang, K. S. Nandakumar, K. F. Liu, L. X. Liu, X. C. Yu, H. J. Tan, C. Zhou, *Phytomedicine* **2019**, *62*, 152965.
[46] M. Ilamathi, S. Santhosh, V. Sivaramakrishnan, *Curr. Top. Med. Chem.* **2016**, *16*, 2453.
[47] X. Chen, E. Song, *Nat. Rev. Drug Discovery* **2019**, *18*, 99.
[48] M. Amano, K. Chihara, K. Kimura, Y. Fukata, N. Nakamura, Y. Matsuura, K. Kaibuchi, *Science* **1997**, *275*, 1308.
[49] H. M. Beere, D. R. Green, *Trends Cell Biol.* **2001**, *11*, 6.
[50] M. Nie, M. S. Balda, K. Matter, *Proc. Natl. Acad. Sci. USA* **2012**, *109*, 10897.
[51] M. Debaugnies, S. Rodríguez-Acebes, J. Blondeau, M.-A. Parent, M. Zocco, Y. Song, V. de Maertelaer, V. Moers, M. Latil, C. Dubois, K. Coulonval, F. Impens, D. Van Haver, S. Dufour, A. Uemura, P. A. Sotiropoulou, J. Méndez, C. Blanpain, *Nature* **2023**, *616*, 168.
[52] T. Yabu, H. Shiba, Y. Shibasaki, T. Nakanishi, S. Imamura, K. Touhata, M. Yamashita, *Cell Death Differ.* **2015**, *22*, 258.
[53] L. Fabbri, A. Chakraborty, C. Robert, S. Vagner, *Nat. Rev. Cancer* **2021**, *21*, 558.
[54] S. M. Fortier, N. M. Walker, L. R. Penke, J. D. Baas, Q. Shen, J. M. Speth, S. K. Huang, R. L. Zemans, A. M. Bennett, M. Peters-Golden, *J. Clin. Investig.* **2024**, *134*, 172826.
[55] Y. Liu, Z. Xun, K. Ma, S. Liang, X. Li, S. Zhou, L. Sun, Y. Liu, Y. Du, X. Guo, T. Cui, H. Zhou, J. Wang, D. Yin, R. Song, S. Zhang, W. Cai, F. Meng, H. Guo, B. o. Zhang, D. i. Yang, R. Bao, Q. Hu, J. Wang, Y. Ye, L. Liu, *J. Hepatol.* **2023**, *78*, 770.
[56] A. Sathe, K. Mason, S. M. Grimes, Z. Zhou, B. T. Lau, X. Bai, A. Su, X. Tan, H. Lee, C. J. Suarez, Q. Nguyen, G. Poultsides, N. R. Zhang, H. P. Ji, *Clin. Cancer Res.* **2023**, *29*, 244.
[57] P. Nallasamy, R. K. Nimmakayala, S. Karmakar, F. Leon, P. Seshacharyulu, I. Lakshmanan, S. Rachagani, K. Mallya, C. Zhang, Q. P. Ly, M. S. Myers, L. Josh, C. E. Grabow, S. K. Gautam, S. Kumar, S. M. Lele, M. Jain, S. K. Batra, M. P. Ponnusamy, *Gastroenterology* **2021**, *161*, 1998.
[58] S. Z. Wu, G. Al-Eryani, D. L. Roden, S. Junankar, K. Harvey, A. Andersson, A. Thennavan, C. Wang, J. R. Torpy, N. Bartonicek, T. Wang, L. Larsson, D. Kaczorowski, N. I. Weisenfeld, C. R. Uytingco, J. G. Chew, Z. W. Bent, C.-L. Chan, V. Gnanasambandapillai, C.-A. Dutertre, L. Gluch, M. N. Hui, J. Beith, A. Parker, E. Robbins, D. Segara, C. Cooper, C. Mak, B. Chan, S. Warrier, et al., *Nat. Genet.* **2021**, *53*, 1334.
[59] A. Bassez, H. Vos, L. Van Dyck, G. Floris, I. Arijs, C. Desmedt, B. Boeckx, M. Vanden Bempt, I. Nevelsteen, K. Lambein, K. Punie, P. Neven, A. D. Garg, H. Wildiers, J. Qian, A. Smeets, D. Lambrechts, *Nat. Med.* **2021**, *27*, 820.
[60] X. Hao, Z. Zheng, H. Liu, Y. Zhang, J. Kang, X. Kong, D. Rong, G. Sun, G. Sun, L. Liu, H. Yu, W. Tang, X. Wang, *Redox Biol.* **2022**, *56*, 102463.
[61] T. Hara, R. Chanoch-Myers, N. D. Mathewson, C. Myskiw, L. Atta, L. Bussema, S. W. Eichhorn, A. C. Greenwald, G. S. Kinker, C. Rodman, L. N. Gonzalez Castro, H. Wakimoto, O. Rozenblatt-Rosen, X. Zhuang, J. Fan, T. Hunter, I. M. Verma, K. W. Wucherpfennig, A. Regev, M. L. Suvà, I. Tirosh, *Cancer Cell* **2021**, *39*, 779.
[62] M. Tajan, M. Hennequart, E. C. Cheung, F. Zani, A. K. Hock, N. Legrave, O. D. K. Maddocks, R. A. Ridgway, D. Athineos, A. Suárez-Bonnet, R. L. Ludwig, L. Novellasdemunt, N. Angelis, V. S. W. Li, G. Vlachogiannis, N. Valeri, N. Mainolfi, V. Suri, A. Friedman, M. Manfredi, K. Blyth, O. J. Sansom, K. H. Vousden, *Nat. Commun.* **2021**, *12*, 366.
[63] C. H. Ly, G. S. Lynch, J. G. Ryall, *Cell Metab.* **2020**, *31*, 1052.
[64] N. Kiweler, C. Delbrouck, V. I. Pozdeev, L. Neises, L. Soriano-Baguet, K. Eiden, F. Xian, M. Benzarti, L. Haase, E. Koncina, M. Schmoetten, C. Jaeger, M. Z. Noman, A. Vazquez, B. Janji, G. Dittmar, D. Brenner, E. Letellier, J. Meiser, *Nat. Commun.* **2022**, *13*, 2699.
[65] O. D. K. Maddocks, C. R. Berkers, S. M. Mason, L. Zheng, K. Blyth, E. Gottlieb, K. H. Vousden, *Nature* **2013**, *493*, 542.
[66] M. E. Pacold, K. R. Brimacombe, S. H. Chan, J. M. Rohde, C. A. Lewis, L. J. Y. M. Swier, R. Possemato, W. W. Chen, L. B. Sullivan, B. P. Fiske, S. Cho, E. Freinkman, K. Birsoy, M. Abu-Remaileh, Y. D.

Shaul, C. M. Liu, M. Zhou, M. J. Koh, H. Chung, S. M. Davidson, A. Luengo, A. Q. Wang, X. Xu, A. Yasgar, L. i. Liu, G. Rai, K. D. Westover, M. G. Vander Heiden, M. Shen, N. S. Gray, et al., *Nat. Chem. Biol.* **2016**, *12*, 452.
[67] A. R. Garcia, M. Arsenian-Henriksson, *Cancer Res.* **2019**, *79*, 3818.
[68] O. Keinan, J. M. Valentine, H. Xiao, S. K. Mahata, S. M. Reilly, M. Abu-Odeh, J. H. Deluca, B. Dadpey, L. Cho, A. Pan, R. T. Yu, Y. Dai, C. Liddle, M. Downes, R. M. Evans, A. J. Lusis, M. Laakso, E. T. Chouchani, M. Rydén, A. R. Saltiel, *Nature* **2021**, *599*, 296.
[69] R. Van Huizen, J. L. Martindale, M. Gorospe, N. J. Holbrook, *J. Biol. Chem.* **2003**, *278*, 15558.
[70] H. A. Hundley, W. Walter, S. Bairstow, E. A. Craig, *Science* **2005**, *308*, 1032.
[71] H. Richly, L. Rocha-Viegas, J. D. Ribeiro, S. Demajo, G. Gundem, N. Lopez-Bigas, T. Nakagawa, S. Rospert, T. Ito, L. Di Croce, *Nature* **2010**, *468*, 1124.
[72] K. E. Bornfeldt, *Circ. Res.* **2000**, *86*, 1101.
[73] H. H. Kampinga, E. A. Craig, *Nat. Rev. Mol. Cell Biol.* **2010**, *11*, 579.
[74] R. Kityk, J. Kopp, I. Sinning, M. P. Mayer, *Mol. Cell* **2012**, *48*, 863.
[75] L. Keller, C. Tardy, L. Ligat, J. Gilhodes, T. Filleron, N. Bery, P. Rochaix, A. Aquilina, S. Bdioui, T. Roux, E. Trinquet, G. Favre, A. Olichon, *Anal. Chem.* **2021**, *93*, 6104.
[76] J. M. Ostrem, U. Peters, M. L. Sos, J. A. Wells, K. M. Shokat, *Nature* **2013**, *503*, 548.
[77] N. Brot, B. Redfield, N. H. Qiu, G. J. Chen, V. Vidal, A. Carlino, H. Weissbach, *Proc. Natl. Acad. Sci. USA* **1994**, *91*, 12120.
[78] D. Zhang, A. M. Li, G. Hu, M. Huang, F. Yang, L. Zhang, K. E. Wellen, X. Xu, C. S. Conn, W. Zou, M. Kahn, S. D. Rhoades, A. M. Weljie, S. Y. Fuchs, N. Amankulor, D. Yoshor, J. Ye, C. Koumenis, Y. Gong, Y. Fan, *Cell Metab.* **2023**, *35*, 517.
[79] A. M. Li, B. He, D. Karagiannis, Y. Li, H. Jiang, P. Srinivasan, Y. Ramirez, M.-N. Zhou, C. Curtis, J. J. Gruber, et al., *Proc. Natl. Acad. Sci. USA* **2023**, *120*, 2302489120.
[80] N. Kiweler, C. Delbrouck, V. I. Pozdeev, L. Neises, L. Soriano-Baguet, K. Eiden, F. Xian, M. Benzarti, L. Haase, E. Koncina, M. Schmoetten, C. Jaeger, M. Z. Noman, A. Vazquez, B. Janji, G. Dittmar, D. Brenner, E. Letellier, J. Meiser, *Nat. Commun.* **2022**, *13*, 2699.
[81] P. Walter, D. Ron, *Science* **2011**, *334*, 1081.
[82] G. Mucciolo, J. Araos Henríquez, M. Jihad, S. Pinto Teles, J. S. Manansala, W. Li, S. Ashworth, E. G. Lloyd, P. S. W. Cheng, W. Luo, A. Anand, A. Sawle, A. Piskorz, G. Biffi, *Cancer Cell* **2024**, *42*, 101.
[83] L. He, Q. Chen, Q. Lu, M. Yang, B. Xie, T. Chen, X. Wang, *Angew. Chem., Int. Ed.* **2024**, *63*, 202404822.
[84] Z. Li, X. Lai, S. Fu, L. Ren, H. Cai, H. Zhang, Z. Gu, X. Ma, K. A. Luo, *Adv. Sci.* **2022**, *9*, 2201734.
[85] W. Xiong, Z. Cheng, H. Chen, H. Liang, M. Wang, Y. Chen, J. Ying, Y. Cai, J. Chai, K. Dou, W. Zheng, S. Zheng, L. Zhao, *Adv. Funct. Mater.* **2024**, *34*, 2410841.
[86] J. Yan, X. Ma, D. Liang, M. Ran, D. Zheng, X. Chen, S. Zhou, W. Sun, X. Shen, H. Zhang, *Nat. Commun.* **2023**, *14*, 6905.
[87] R. Kalluri, *Nat. Rev. Cancer* **2016**, *16*, 582.
[88] R. Rosenzweig, N. B. Nillegoda, M. P. Mayer, B. Bukau, *Nat. Rev. Mol. Cell Biol.* **2019**, *20*, 665.
[89] H. Li, Q. Luo, H. Zhang, X. Ma, Z. Gu, Q. Gong, K. Luo, *Chem. Soc. Rev.* **2023**, *52*, 47.
[90] G. Manca, L. M. Garau, S. Mazzarri, L. Mazzuca, S. Muccioli, M. Ghilli, G. Naccarato, P. M. Colletti, D. Rubello, M. Roncella, et al., *Clin. Nuclear Med.* **2021**, *46*, 181.
[91] J. K. A. Rinne, H. Huhta, T. Pinta, A. Turunen, A. Mattila, K. Tahkola, O. Helminen, P. Ohtonen, T. Rautio, J. Kössi, *JAMA, J. Am. Med. Assoc.* **2025**, *160*, 486.
[92] A. H. Slyper, *JAMA, J. Am. Med. Assoc.* **1994**, *272*, 305.
[93] L. H. Block, A. Pletscher, *Trends Pharmacol. Sci.* **1988**, *9*, 214.
[94] X. Liu, Y. Cai, Y. Zhang, H. Zhang, S. Tian, Y. Gong, Q. Song, X. Chen, X. Ma, Y. Wen, Y. Chen, J. Zeng, *Pharmacolog. Res.* **2024**, *210*, 107526.
[95] D. Timothy, P. Hoang, I. K. L., H. N. F., B. K. C., P. V. u. D. T., P. S. B., T. H. M., B. Tran, *Antimicrob. Agents Chemother.* **2001**, *45*, 181.
[96] W. Zhang, M. Xia, J. Li, G. Liu, Y. Sun, X. Chen, J. Zhong, *Mol. Med.* **2025**, *31*, 146.
[97] M. Ran, Y. Deng, J. Yan, A. Zhang, Y. Wei, X. Li, H. He, J. Gou, T. Yin, X. Tang, J. Kong, H. Zhang, H. Zhang, Y. Zhang, *Chem. Eng. J.* **2022**, *450*, 138291.
[98] T. Thoudam, D. Chanda, I. S. Sinam, B.-G. Kim, M.-J. Kim, C. J. Oh, J. Y. Lee, M.-J. Kim, S. Y. Park, S. Y. Lee, M.-K. Jung, J. Y. Mun, R. A. Harris, N. Ishihara, J.-H. Jeon, I.-K. Lee, *Proc. Natl. Acad. Sci. USA* **2022**, *119*, 2120157119.
[99] A. M. Race, I. B. Styles, J. Bunch, *J. Proteom.* **2012**, *75*, 5111.
[100] K. D. Bemis, A. Harry, L. S. Eberlin, C. Ferreira, S. M. van de Ven, P. Mallick, M. Stolowitz, O. Vitek, *Bioinformatics* **2015**, *31*, 2418.
[101] G. Wang, B. Heijs, S. Kostidis, A. Mahfouz, R. G. J. Rietjens, R. Bijkerk, A. Koudijs, L. A. K. van der Pluijm, C. W. van den Berg, S. J. Dumas, P. Carmeliet, M. Giera, B. M. van den Berg, T. J. Rabelink, *Nat. Metab.* **2022**, *4*, 1109.
[102] D. M. Cable, E. Murray, L. S. Zou, A. Goeva, E. Z. Macosko, F. Chen, R. A. Irizarry, *Nat. Biotechnol.* **2022**, *40*, 517.
[103] Y. Zhou, B. Zhou, L. Pache, M. Chang, A. H. Khodabakhshi, O. Tanaseichuk, C. Benner, S. K. Chanda, *Nat. Commun.* **2019**, *10*, 1523.